

# POPULATION DIAGRAM ANALYSIS OF LINE EMISSION FROM MOLECULAR CLOUDS

Paul F. Goldsmith<sup>1</sup>

National Astronomy and Ionosphere Center, Department of Astronomy, Cornell University,  
Ithaca NY 14853

William D. Langer<sup>2</sup>

MS 169-506, Jet Propulsion Laboratory, California Institute of Technology,  
Pasadena CA 91109

## ABSTRACT

We develop the use of the population diagram method to analyze molecular emission in order to derive physical properties of interstellar clouds. We focus particular attention on how optical depth affects the derived total column density and the **temperature distribution**. We present analytic results for linear molecules in *LTE*. We investigate numerically how subthermal excitation influences the population diagram technique, studying how the determination of kinetic temperature is affected when the local density is insufficient to achieve *LTE*. We present results for  $HC_3N$  and  $CH_3OH$ , representative of linear and non-linear molecules, respectively. In some cases, alternative interpretations to the standard optically thin and thermalized picture yield significantly different results for column density and kinetic temperature, and we discuss this behavior. The population diagram method can be a very powerful tool for determining physical conditions in dense clouds if proper recognition is given to effects of saturation and subthermal excitation. We argue that the population diagram technique is, in fact, superior to fitting intensities of different transitions directly, and indicate how it can be effectively employed.

*excitation analysis*

*Subject headings:* ISM: interstellar clouds – ISM: molecules – temperature

---

<sup>1</sup>pfg@astrosun.tn.cornell.edu

<sup>2</sup>langer@nimba.jpl.nasa.gov

## 1. Introduction

Molecular line emission can yield important information about physical conditions in dense interstellar clouds. The column density of the species being observed and the cloud kinetic temperature can most straightforwardly be determined; indeed, under certain conditions, these parameters can be obtained from observation of a single transition. Other important characteristics of clouds such as their density, velocity structure, and the magnetic field distribution, can be obtained only by observing multiple transitions, making maps, or employing specialized types of observations.

However, the validity of even the apparently simpler techniques needs to be demonstrated. For example, a single transition, if optically thick and thermalized, can provide the kinetic temperature ( $T_K$ ) of the gas at a location in the cloud where  $\tau \simeq 1$ . In the case of carbon monoxide, the optical depth of the common isotopic species can be checked by observing rarer isotopomers, while the thermalization can be evaluated by an approximate comparison of density (determined from a different technique) with the relatively low spontaneous decay rates of the lower rotational transitions. The confidence developed in this approach has led to the widespread use of  $^{12}\text{CO}$  as a probe of the kinetic temperature in molecular clouds. It is useful in this application, even though observational results as well as theoretical models suggest that there are significant variations of the kinetic temperature as a function of position within molecular clouds.

An optically thin transition produces an antenna temperature which is proportional to the column density in the upper level of the transition being observed, and if all transitions are thermalized, and we know the kinetic temperature, we can convert the single measured column density into the column density of the species in question. Some of the early spectral surveys of emission from molecular clouds provided the first instance in which a sufficient number of transitions were observed that an analysis of the excitation, or at least a check for self-consistency of the assumptions of optical thinness and thermalization, was possible.

One potentially important and frequently adopted technique to analyze cloud properties from molecular line emission is the “rotation diagram”. This term refers to a plot of the column density per statistical weight of a number of molecular energy levels, as a function of their energy above the ground state. In local thermodynamic equilibrium (*LTE*), this will just be a Boltzmann distribution, so a plot of the natural logarithm of  $N_u/g_u$  versus  $E_u/k$  will yield a straight line with a slope of  $1/T$ , where  $g_u$  is the statistical weight of the level  $u$  and  $E_u$  is its energy above the ground state. The temperature inferred is often called the “rotational temperature”, although it is not *a priori* restricted to a set of rotational energy levels. The temperature obtained would be expected to be equal to the kinetic

temperatures if all levels were thermalized.

Linke, Frerking, & Thaddeus (1979) were among the first to apply this approach to determine the kinetic temperature in Sgr B2 using six rotational lines of  $CH_3SH$  (methyl mercaptan). They fit a linear function to their plot of log intensity versus energy to derive a rotational temperature of 9 K, considerably lower than estimates of the kinetic temperature using tracers such as  $^{12}CO$ . A similar result,  $T = 14$  K, was derived by Frerking, Linke, & Thaddeus (1979) using the linear molecule  $HNCS$  (isothiocyanic acid). It is difficult to understand how a hot region such as Sgr B2 could have such a low kinetic temperature unless these species trace a particularly cold sub-condensation. A very extensive application of this approach was made much later by Turner (1991) using 36 species (including over 700 lines) in Sgr B2 and 27 species (responsible for over 800 lines) in Orion KL. Turner noted problems with using some of this data, as the assumption of optically thin emission appears to break down. Turner fit most of the rotational diagrams with a single straight line although in a few cases the data fell into two categories and two separate fits were made. In almost all cases the data have a considerable scatter around the fit and in many (if not most) cases it is not clear that a single or even a piecewise linear fit is satisfactory. The rotational temperatures he found range from 9 K to over 200 K in Sgr B2 and 12 K to 120 K in OMC1.

The rotation diagram approach was also used by Sutton *et al.* (1995) to derive the kinetic temperature in their study of the distribution of molecules in the core of OMC -1. These authors found that the molecular excitation can be reasonably well described by rotational temperatures 15 – 45 K for the extended ridge, 50-180 K for the hot core, and 50 –130 K for the compact ridge and the plateau. A similar approach was taken by Serabyn & Weisstein (1995) to derive temperatures in the OMC core.

In addition to hot star forming cores there are many other structural and morphological features associated with the star formation process, including cold dark cores, molecular outflows, jets, disks, and ultracompact HII regions. It is important to determine the kinetic temperatures within all of these features to study the energetics and interactions in star forming regions. In the case of the high mass protostar IRAS 20126+4104, Cesaroni *et al.* (1997) have attempted to derive the kinetic temperature for the disk outflow region using a rotational diagram. They observed emission from many levels of  $CH_3CN$  (methyl cyanide) and  $CH_3OH$  (methanol) and derived temperatures of  $\simeq 50$  K for the bulk of the gas and 150–260 K for the core. However, the data show a great deal of scatter and are far from linear over a wide range of excitation energy.

In all of these studies, the total column density of each species has associated with it an uncertainty that is closely tied to the assumption of complete thermalization and the value of the inferred temperature. An additional error arises if the emission is not optically

thin. To first order, this produces an underestimate in the upper level column density of the observed transition, but this can also produce a more insidious error in the rotational temperature determined (which again impacts the total column density of the species in question).

In this paper we examine the conditions and assumptions used to derive column densities, rotational temperatures, and thus the kinetic temperature, using what we prefer to call the “population diagram” method. We feel that this correctly reflects the idea of analyzing the populations of the various levels in a direct, graphical way. There are many situations where the assumption of optically thin lines may not hold. The observer in general is unaware whether the lines observed *appear* optically thin because their opacity is truly small, or because the emission is beam diluted (as could result from a highly clumped structure, for example). If a number of observed transitions do make a straight line in a population diagram where  $\log(\text{Integrated Intensity per Statistical Weight})$  is plotted against  $E_u$ , general practice has been to conclude that all levels are thermalized, and that the excitation temperature is equal to the kinetic temperature. This important assumption also deserves investigation.

In Section 2 of this paper we review the relationship between line emission and the observed antenna temperature, and discuss various limiting cases. In Section 3 we investigate how the integrated intensity, the upper level column density, and the total molecular column density are related in various situations. In Section 4 we discuss the Population Diagram, and the effects of finite optical depth when level populations are in *LTE*. We treat the case of linear molecules in some detail as analytic expressions are straightforward to obtain, and use methanol as an example of a more complex molecular species. In Section 5 we consider non-*LTE* excitation for both linear and more complex molecules, and discuss effects on the population diagram. In Section 6 we discuss some uses of the population diagram and indicate some of the advantages it offers for determination of the hydrogen density from multi-transition observations of molecular clouds.

## 2. Line Emission and Antenna Temperature

### 2.1. General Relationships

The antenna temperature  $T_a$  produced at a frequency  $\nu$  by a source having brightness distribution  $B_\nu(\theta, \phi)$  is given by

$$T_a = (A_e/2k) \int_{4\pi} B_\nu(\theta, \phi) P_n(\theta, \phi) d\Omega, \quad (1)$$

where  $P_n(\theta, \phi)$  is the normalized power pattern of the antenna. This function describes the relative response of the antenna to signals coming from different directions, normalized such that on boresight, the direction of maximum response,  $P_n(0, 0) = 1$ , and  $\int_{4\pi} P_n(\theta, \phi) d\Omega = \Delta\Omega_a$ , the antenna solid angle. The integral in equation 1 can be conveniently expressed in terms of a source–antenna coupling factor if the source and antenna power pattern have some symmetry or other simplifying properties. Two limiting cases illustrate the behavior of equation 1: a point source and uniform emission filling the antenna beam.

Taking the solid angle subtended by a “pointlike” source to be much smaller than  $\Delta\Omega_a$ , we can take  $P_n$  to be equal to unity over the solid angle of the source. Further, if the source is uniform,  $B_\nu$  can be removed from the integral, which is then the source solid angle  $\Delta\Omega_s$ . In this situation we can write

$$T_a = (A_e/2k)(\Delta\Omega_a)\left[\frac{\Delta\Omega_s}{\Delta\Omega_a}\right]B_\nu, \quad (2)$$

where the expression in square brackets is the beam dilution factor.

From the “antenna theorem” (Kraus 1966),  $A_e\Delta\Omega_a = \lambda^2$ , so that we can rewrite equation 2 as

$$T_a = (\lambda^2/2k)\left[\frac{\Delta\Omega_s}{\Delta\Omega_a}\right]B_\nu. \quad (3)$$

If an extended source is uniform over the antenna solid angle, we can take  $B_\nu$  out of the integral in equation 1, which then becomes  $\Delta\Omega_a$ . The antenna theorem then gives us  $T_a = (\lambda^2/2k)B_\nu$ . The beam dilution factor is thus much less than unity for very small sources, and reaches a maximum value of unity for an extended, uniform source.

The brightness produced by a source at temperature  $T$  having optical depth  $\tau$  is

$$B_\nu = \frac{h\nu/k}{e^{h\nu/kT} - 1} [1 - e^{-\tau}]. \quad (4)$$

However, for reasons that will become clear momentarily, it is convenient to write this as

$$B_\nu = \frac{h\nu/k}{e^{h\nu/kT} - 1} \left[ \frac{1 - e^{-\tau}}{\tau} \right] \tau. \quad (5)$$

We can write the optical depth of the transition as

$$\tau = \frac{h}{\Delta v} N_u B_{ul} [e^{h\nu/kT} - 1], \quad (6)$$

where  $B_{ul}$  is the Einstein  $B$ -coefficient for the transition, and  $\Delta v$  is the line width in velocity. (More exactly, we should employ the line profile function evaluated at the peak of the line, but this is very close to  $\Delta v^{-1}$  for a Gaussian or similar line profile.)

Substituting equations (6) and (5) into equation (3), together with the relationship that  $B_{ul} = A_{ul}c^3/8\pi h\nu^3$ , we obtain

$$T_a = \frac{hc^3 N_u A_{ul}}{8\pi k\nu^2 \Delta v} \left[ \frac{\Delta\Omega_s}{\Delta\Omega_a} \right] \left[ \frac{1 - e^{-\tau}}{\tau} \right]. \quad (7)$$

Note that this expression does **not** explicitly include the temperature of the source.

We can invert equation 7 to yield an expression for the upper level column density in terms of the observed quantity,  $T_a$ . It is often convenient to consider the integrated line intensity,

$$W = \int T_a dv, \quad (8)$$

which in our usage is just  $T_a \Delta v$ , to obtain

$$N_u = \frac{8\pi k\nu^2 W}{hc^3 A_{ul}} \left[ \frac{\Delta\Omega_a}{\Delta\Omega_s} \right] \left[ \frac{\tau}{1 - e^{-\tau}} \right]. \quad (9)$$

## 2.2. Limiting Cases

Different analysis techniques, including population and rotation diagram analysis, have as inputs the upper level column density. It is a considerable simplification to make the two assumptions that: **(1) the source fills the beam, and (2) the emission is optically thin**. If these are both satisfied, each of the two expressions in square brackets in equation 9 is equal to unity, and we obtain the relationship

$$N_u^{thin} = \frac{8\pi k\nu^2 W}{hc^3 A_{ul}}, \quad (10)$$

which can often be found in the literature. We define  $\gamma_u$  to be the combination of constants relating the integrated intensity and the upper level column density in this limit. Thus we have

$$\gamma_u = \frac{8\pi k\nu^2}{hc^3 A_{ul}}, \quad (11)$$

and

$$N_u^{thin} = \gamma_u W. \quad (12)$$

This useful result can also be obtained starting with the basic definition of brightness of an optically thin source ignoring any background radiation,

$$B_\nu = \frac{A_{ul} N_u^{thin} h\nu}{4\pi\Delta\nu} = \frac{A_{ul} N_u^{thin} hc}{4\pi\Delta\nu}. \quad (13)$$

This yields

$$T_a = \frac{hc^3 A_{ul} N_u^{thin}}{4\pi\nu^2\Delta\nu}, \quad (14)$$

or

$$W = \frac{A_{ul} hc^3 N_u^{thin}}{8\pi k\nu^2} = \frac{N_u^{thin}}{\gamma_u}, \quad (15)$$

which is just the inverse of equation 12.

If the first assumption is not valid and the source does not fill the beam, then the correct upper level column density is greater than that obtained assuming the beam to be filled by a factor equal to  $\Delta\Omega_a/\Delta\Omega_s$ . This correction can be substantial, but can only be tested definitively by observing with higher angular resolution. In this section, we will assume that the source uniformly fills the antenna beam, and return to this issue in Section 6.2.

We now consider possibly optically thick emission, but since we are assuming that the source does fill the antenna beam, we set  $\Delta\Omega_a/\Delta\Omega_s = 1$  in equation (9). We define the optical depth correction factor  $C_\tau$ ,

$$C_\tau = \frac{\tau}{1 - e^{-\tau}}, \quad (16)$$

and we find that

$$N_u = \gamma_u W C_\tau = N_u^{thin} C_\tau. \quad (17)$$

The optical depth correction factor defined here is greater than or equal to unity. It is the factor by which the upper level column density derived from observed integrated intensity  $W$  *would appear* to be too small as a result of the finite optical depth. Hence, to obtain the correct value of  $N_u$ , we must multiply  $N_u^{thin}$  by  $C_\tau$  as indicated in equation 17.

Direct determination of the optical depth by comparison with emission from other isotopomers, measurement of hyperfine ratios, or other means, is rarely straightforward. We will show below, how the "population diagram" can also be used as a diagnostic of the optical depth of the emission.

### 3. Relating Upper Level and Total Column Densities

To understand different possible behavior in the "population diagram", we need to be able to calculate  $W$  for each level, and then see what value of  $N_u$  is found and how it depends on the energy of the transition, as well as on other factors.

#### 3.1. Non-LTE Excitation

In the case of arbitrary excitation, a different temperature may characterize the population of *each* level relative to that of the ground state or relative to that of any other level. The excitation temperature  $T_{ex}$  is defined by the relative populations or column densities of any two levels  $i$  and  $j$  of statistical weights  $g_i$  and  $g_j$  and energies  $E_i$  and  $E_j$  relative to an arbitrary common reference, through

$$\frac{N_j}{N_i} = \frac{g_j}{g_i} \exp[-(E_j - E_i)/kT_{ex}]. \quad (18)$$

The excitation temperature can be defined whether or not the two levels in question are connected by a radiative transition, although it is only in this situation that  $T_{ex}$  can be directly measured.

#### 3.2. LTE

For a molecule in local thermodynamic equilibrium (LTE), all excitation temperatures are the same, and taking this to be given by  $T$ , the population of each level is given by

$$N_u = \frac{N}{Z} g_u e^{-E_u/kT}, \quad (19)$$



where  $N$  is the total column density of the species in question, and  $Z$  is the partition function, given by

$$Z = \sum_{\text{all levels}} N_i. \quad (20)$$

In *LTE* it is straightforward to obtain the total molecular column density from the column density of any individual transition if  $T$  is known. If the molecule's transitions are not thermalized, the fractional population of a given level can be greater or less than that in *LTE*, so it is difficult to make a general statement about how the determination of the total column density is affected. We will return to this topic in Section 5.

#### 4. The Population Diagram

A population diagram can be useful to assess whether the emission is optically thick or thin, whether the level populations are described by *LTE*, and to determine what temperature describes the population distribution in the event that *LTE* applies.

##### 4.1. Population Diagram and *LTE*

The “traditional” rotation diagram is based on the supposition that all level populations are described by *LTE*. We then rewrite equation 19 to obtain

$$\ln \frac{N_u}{g_u} = \ln N - \ln Z - \frac{E_u}{kT}. \quad (21)$$

We can also include the possibility of finite optical depth explicitly using equation 17

$$\ln \frac{N_u^{thin}}{g_u} + \ln C_\tau = \ln N - \ln Z - \frac{E_u}{kT}. \quad (22)$$

If the optical depth is small,  $C_\tau$  is unity, and from equation 17,  $N_u = N_u^{thin}$ . Thus, the logarithm of the upper level column density per statistical weight does show a linear dependence on upper level energy. This is directly translatable to an observational relationship through equation 10, giving us

$$\ln \frac{\gamma_u W}{g_u} = \ln N - \ln Z - \frac{E_u}{kT}. \quad (23)$$

If the optical depth is *not* small compared to unity, then we must use equation 22, which can be written in terms of the observed  $W$  as,

$$\ln \frac{\gamma_u W}{g_u} = \ln N - \ln C_\tau - \ln Z - \frac{E_u}{kT}. \quad (24)$$

If we were not aware of the finite optical depth and thus took  $C_\tau$  equal to 1, each of the upper level populations would be **underestimated by a factor  $C_\tau$** . The ordinate of the population diagram would consequently be below its correct value by an amount  $\ln C_\tau = \ln \frac{\tau}{1-e^{-\tau}}$ .

#### 4.2. Optical Depth for Rotational Transitions of Linear Molecules

For a linear molecule we can label each state by its rotational quantum number,  $J$ , its energy,  $E_J = hB_0J(J+1)$ , and its statistical weight,  $g_J = 2J+1$ . The frequency of the transition  $J \rightarrow J-1$  is given by  $\nu_{J,J-1} = 2B_0J$ , the corresponding Einstein  $A$ -coefficient is given by

$$A_{J,J-1} = \frac{64\pi^4 \nu^3 \mu^2}{3hc^3} \frac{J}{2J+1}, \quad (25)$$

and the Einstein  $B$ -coefficient is

$$B_{J,J-1} = \frac{8\pi^3 \mu^2}{3h^2} \frac{J}{2J+1}. \quad (26)$$

We can write the optical depth of the transition  $J \rightarrow J-1$  as

$$\tau_{J,J-1} = \frac{8\pi^3 \mu^2}{3h} \frac{N}{\Delta\nu} \frac{1}{Z} J e^{-aJ(J+1)} (e^{2aJ} - 1). \quad (27)$$

#### 4.3. Linear Molecules in *LTE*

If *LTE* applies, and we are in a relatively warm cloud so that  $kT > hB_0$ , making the substitution  $u = J(J+1)$  and defining

$$a = hB_0/kT, \quad (28)$$

we can transform the partition function into an integral:

$$Z = \sum_{J=0}^{J=\infty} (2J+1)e^{-hB_0J(J+1)/kT} \rightarrow \int_0^{\infty} e^{-au} du. \quad (29)$$

This yields the simple result that  $Z = a^{-1} = kT/hB_0$ , which is surprisingly accurate even for temperatures as low as  $T \sim B_0/2k$ .

The variation of  $\tau$  as a function of energy and  $J$  for a linear molecule in *LTE* is given by equation (27) with  $Z = a^{-1}$ . It is shown in Figure 1, which gives the relative values of the optical depths of the different transitions as a function of  $J$  of the upper level.

For  $a < 1$ , the optical depth exhibits a peak at a value of  $J$  which we take to be equal to  $J_{max \tau}$ . If we are in the limit  $aJ_{max \tau} < 1$ , the value of  $J_{max \tau}$  is given by

$$J_{max \tau} = 1/\sqrt{a} = \sqrt{kT/hB_0}. \quad (30)$$

The energy of the transition having maximum optical depth is just  $E_{max \tau} = hB_0J_{max \tau}(J_{max \tau} + 1)$ , and for  $J_{max \tau} > 1$ , we find the plausible result that

$$E_{max \tau} = kT. \quad (31)$$

The frequency of the transition of maximum opacity is then

$$\nu_{max \tau} = 2B_0J_{max \tau} = 2B_0/\sqrt{a}. \quad (32)$$

A convenient conversion factor is

$$a = 0.048B_0(GHz)/T(K) \quad (33)$$

so that

$$J_{max \tau} = 4.6\sqrt{T(K)/B_0(GHz)}, \quad (34)$$

and

$$\nu_{max \tau}(GHz) = 9.13\sqrt{T(K)B_0(GHz)}. \quad (35)$$

These expressions give an idea of which transition, at what frequency, will suffer the most from the effect of optical depth. For example, for  $HC_3N$  having  $B_0 \simeq 4.6 GHz$ , for  $T = 10 K$ ,  $J_{max \tau} = 7$  and  $\nu_{max \tau} = 61 GHz$ . This suggests that for somewhat warmer clouds, the  $\lambda \simeq 3 mm$  transitions of this molecular species will be the most affected by optical depth effects.

#### 4.4. Effect of Optical Depth and The Optical Depth Correction Factor for Linear Molecules Having Finite Values of $\tau$

In Figure 2 we present population diagrams calculated for the molecule  $HC_3N$ , which has rotation constant  $B_0 = 4.55 \text{ GHz}$  and permanent electric dipole moment  $\mu = 3.72 \text{ D}$  (Lafferty & Lovas (1978)). For the example shown with  $T_K = 22\text{K}$ ,  $a = hB_0/kT = 0.01$ , and a hydrogen density of  $10^9 \text{ cm}^{-3}$  is sufficient to thermalize all of the transitions with significant population. These calculations were carried out using a large velocity gradient radiative transfer code, for which, in addition to the hydrogen density and kinetic temperature, the input needed is the fractional abundance per velocity gradient of the species being studied. This quantity, when multiplied by the hydrogen density, is equal to the column density of the species in question per unit line width, which determines the optical depth in any model. A velocity gradient of  $1 \text{ km s}^{-1}/pc$  or line width equal to  $1 \text{ km s}^{-1}$  and size equal to  $1 pc$  are typical for molecular clouds, and in this case the fractional abundance per unit line width is numerically equal to the fractional abundance itself. We shall in the following refer to fractional abundances rather than fractional abundances per unit line width, when there is no danger of confusion, and adopt a line with of  $1 \text{ km s}^{-1}$  where a specific value is required.

For the lowest value of the fractional abundance,  $10^{-15}$ , we do indeed see a linear curve as expected from optically thin emission from a molecule in *LTE*. When the fractional abundance is increased by a factor of 10, the curve has moved up by close to this factor, and is still nearly linear. As the fractional abundance increases further, the curves become highly nonlinear and lie well below the values that would be extrapolated from the optically thin results. The divergence from linear behavior is most striking for transitions with  $3 \leq J_u \leq 12$ , which is the range for which the optical depths are largest.

Once a particular transition has become optically thick, the value of  $\gamma_u W/g_u$  cannot increase further, and in comparing the results for the two largest fractional abundances, we see that there is a small change only for the  $J = 1 \rightarrow 0$  transition, which has the lowest optical depth of all those considered. Thus, changing the  $HC_3N$  fractional abundance from  $10^{-12}$  to  $10^{-11}$  has essentially no effect, as all transitions are already optically thick for the lower value.

The limiting form of the population diagram when all transitions are optically thick is determined by the fact that the antenna temperature is that produced by a blackbody. In the Rayleigh–Jeans limit, this yields (with  $a$  defined in equation 28)

$$\frac{\gamma W}{g_u} = \frac{2\Delta\nu}{16\pi^3\mu^2} \frac{1}{aJ^2}, \quad (36)$$

where  $\delta\nu$  is the line width. The nonlinear behavior on the semi-log plot can have several different effects, which appear even in the case for moderate fractional abundance when all transitions except for the lowest and highest are optically thick. From Figure 2, with incomplete and necessarily imperfect data, it would be possible to conclude that two different temperature components were present, while in fact one is seeing the effect of the finite opacity. For example, with  $X = 10^{-13}$ , if one fits the five lowest transitions, one obtains an anomalously low temperature of 6.5 K, while using the five highest transitions included in Figure 2, one obtains the erroneously high value of 51 K (compared to the actual value of 22K). This effect is even more extreme for higher optical depths, and while the predicted intensities for lower values of  $J$  are less linear, it would be possible to think, if one were not aware of the large values of the optical depth, that a fraction of the gas were thermalized at a very low temperature. For very high values of  $J$ , the level populations drop and the transitions become optically thin, which results in these points falling on a line consistent with the correct temperature.

If not properly accounted for, the finite optical depth results in an underestimate of the total molecular column density. The situation is complicated by the fact that a linear fit would evidently not be satisfactory for the full range of transitions included in Figure 2. If we ignore the finite optical depth, we would use equation 21, which gives that the value of the ordinate extrapolated to zero upper state energy is equal to  $N/Z$ . The different temperatures that one would derive from straight lines fit to the different sections of the curve also enter through the fact that the partition function is proportional to the temperature derived. For a fractional abundance per unity velocity gradient of  $10^{-13}(kms^{-1}/pc)^{-1}$  and a line width of  $1 kms^{-1}$ , the total  $HC_3N$  column density is  $3.08 \times 10^{14} cm^{-2}$ . Using only the data from the lower  $J$  transitions, we find  $\ln(N/Z)$  equal to 28.7, and with the derived temperature of 6.5 K, we obtain  $N = 9 \times 10^{13} cm^{-2}$ . For the highest five transitions, we obtain, with the derived temperature of 51 K,  $N = 1 \times 10^{14} cm^{-2}$ .

In both of these cases we have assumed that *all* levels are characterized by the parameters derived from the limited range of  $J$ . The lower transitions give an intercept which is not far from the value extrapolated from optically thin results, but the erroneously low temperature results in a column density which is too low by almost a factor of 3.5. If the higher  $J$  transitions are used, the intercept is dominated by these very optically thick lines, and the erroneously high temperature only partially compensates, with the final result being too low by approximately a factor of three. The maximum value of  $\tau$  in this example is 3.8, and from equations 16 and 17, we would anticipate an underestimate of the upper state column densities in the middle  $J$  range of approximately this factor. We see that since these levels are those which do have a large fraction of the total molecular population, the total column

density is underestimated by a factor only slightly less than the peak optical depth.

In Figure 3 we show more generally the effect of omitting the optical depth correction factor, in terms of how it would affect the left hand side of a population diagram such as that indicated in equation 24. If we ignored the finite optical depth issue, the observationally determined integrated intensities directly give the upper level column densities, which would exhibit a Boltzmann distribution, characterized by a straight line on a semi-log plot. We have plotted the negative of the natural logarithm of the optical depth correction factor so that the appearance of the curves mimics the effect on the relationship in a population diagram.

Figure 3 shows  $C_\tau$  for three different values of  $hB_0/kT$ , which is equal to 0.001 in Figure 3a, 0.01 in Figure 3b, and 0.1 in Figure 3c. The energy of the transition having the maximum optical depth is always given by equation 31. We see that the form of the variation of  $C_\tau$  as a function of optical depth is essentially independent of  $E_u/kT$ , but that the quantitative behavior *does* depend on this parameter. For fixed molecular parameters and column density, the maximum value of  $\tau$  varies as  $a$  (in the limit  $a < 1$ ). However, the optical depth of the  $J = 1$  to  $J = 0$  transition varies as  $a^2/e$  in this same limit, so that the ratio of the optical depth of the most optically thick transition to that of the  $J = 1$  to 0 transition is

$$\frac{\tau_{max}}{\tau_{1,0}} = \frac{1}{ea}, \quad (37)$$

again in the limit  $a < 1$ . This result is confirmed by numerical calculations to be quite accurate for  $a$  as small as 0.1. For a given value of  $\tau_{1,0}$ , as  $a$  ( $= hB_0/kT$ ) increases, the level having maximum  $\tau$  decreases, as does the maximum value of  $\tau$ . Hence, for the same value of  $\tau_{1,0}$ , the correction factors seen in Figures 3b and 3c are closer to unity than those in Figure 3a.

#### 4.5. Nonlinear Molecules in LTE

A wide variety of molecules have been detected in interstellar clouds, with many having more complex energy level structures than the simple linear molecules discussed above. In general, there can be several transitions from a given state, and the dependence of transition frequencies on the energy of the upper state is more complex.

Here we give some results for the  $E$  species of  $CH_3OH$ , a molecule that has relatively large abundances in dense clouds, and has been found to have an enhanced abundance in outflows. The energy levels, labeled by  $J$  and  $K$ , are shown in Figure 4, along with representative transitions, which obey the selection rules  $\Delta J, \Delta K = 0, \pm 1$ . However, due to

the asymmetry in the energy levels with respect to the sign of  $K$ , “ladders” having different values of  $K$  have quite different arrangements of allowed transitions. In particular, states with  $K = 3$  and  $K = -3$  (excepting the lowest ones) have (in addition to a transition with  $\Delta K = 0$ ), two strong downwards transitions with relatively large frequencies, resulting in *total* spontaneous decay rates between  $10^{-3}s^{-1}$  and  $10^{-2}s^{-1}$  for the levels considered here. The  $K = -1$  levels have, in contrast, only two downwards transitions and total spontaneous decay rates that do not exceed a few  $\times 10^{-4}s^{-1}$ . As a result, the  $H_2$  densities required to thermalize the various level populations are quite different.

The different transitions also have very different absorption coefficients, so that their optical depths vary considerably for a given molecular abundance. With the collision rate coefficients adopted here (discussed in Section 5.3) hydrogen densities greater than  $10^9 \text{ cm}^{-3}$  are required to bring all of the transitions considered here into *LTE*. Population diagrams for  $n(H_2) = 10^9 \text{ cm}^{-3}$  as a function of fractional abundances of  $CH_3OH$  are shown in Figure 5. As for the previous example, we adopt a velocity gradient of  $1 \text{ km s}^{-1}/pc$  and a line width of  $1 \text{ km s}^{-1}$ , and refer to the fractional abundances, which are numerically equal to the fractional abundances per unit velocity gradient. For the lowest abundance considered in Figure 5,  $X(CH_3OH) = 10^{-14}$ , all transitions are optically thin and we obtain a straight line corresponding to the kinetic temperature of  $50 \text{ K}$ . Note that since all opacities are  $\ll 1$ , the various transitions with a common upper level all appear as a single point on the straight line. As the fractional abundance increases, the transitions with greater absorption coefficients become optically thick, and for  $X(CH_3OH) = 10^{-12}$ , we see that a number of transitions have upper level populations significantly below those extrapolated from optically thin results. For  $X(CH_3OH) = 10^{-11}$  we see a greatly enhanced apparent “scatter” in the population diagram, since some transitions have clearly reached their optically thick limiting value, while others, defining the upper edge of the envelope, are still close to being optically thin.

For a species with complex energy level structure such as  $CH_3OH$ , it is difficult to draw simple, general conclusions about the effect of finite  $\tau$ , as is possible for linear molecules. Our modeling suggests that optically thick emission even in *LTE* can significantly increase the scatter in the data if a mixture of thin and thick transitions are included. Given that the transitions we consider cover frequencies between  $6.9 \text{ GHz}$  and  $633 \text{ GHz}$ , actual data sets may not see only an increased scatter, but could instead indicate erroneous temperatures and column densities, depending on which particular transitions are included. Thus, the potentially deleterious effect of uncorrected optical depths should not be ignored for more complex molecules.

## 5. Non-*LTE* Excitation

We next examine what happens if the hydrogen density is insufficient to thermalize some, or all of the transitions, so that the populations of the energy levels used in forming the population diagram cannot be described by *LTE*. We restrict ourselves again only to the case of  $HC_3N$  as representative of linear molecules, and  $CH_3OH$  as an example of more complex molecular species.

### 5.1. Linear Molecules

For the calculations described in this section we have used the collision rate coefficients of Green & Chapman (1978), which include the lowest 24 levels of  $HC_3N$ . We have not explicitly included a correction for  $H_2$  rather than  $He$  as collision partner, which would reduce the actual density corresponding to each density given by approximately 50 percent. In Figure 6 we show results for densities between  $10^3$  and  $10^8 \text{ cm}^{-3}$ . The fractional abundance of  $HC_3N$  per unit velocity gradient is  $10^{-15}(\text{km s}^{-1}/pc)^{-1}$  which results in all transitions being optically thin for all  $H_2$  densities. For densities  $\geq 10^6 \text{ cm}^{-3}$ , the populations of the levels considered here are thermalized, so that the population diagrams are essentially straight lines corresponding to the kinetic temperature of 22 K.

The behavior for lower densities is more surprising, however. While none of these curves forms a perfect straight line as do the ones for higher densities, for a significant range of energies (excepting the lowest transitions), each can be fit satisfactorily with a straight line. The temperatures implied are 6 K for  $n(H_2) = 10^3 \text{ cm}^{-3}$ , 7 K for  $n(H_2) = 10^4 \text{ cm}^{-3}$ , and 8 K for  $n(H_2) = 10^5 \text{ cm}^{-3}$ . All of these are decisively subthermal, and yet it would be difficult to recognize this unless we had data that included the transitions for  $J \leq 6$  and  $J > 20$ . However, the latter would be relatively weak under these conditions, and thus difficult, or impossible, to observe.

The results seen here are unexpected because the range of spontaneous decay rates for the levels considered here is very large. From equation 25 we find that  $A_{1,0} = 4 \times 10^{-8} \text{ s}^{-1}$ ,  $A_{6,5} = 1.1 \times 10^{-5} \text{ s}^{-1}$ , and  $A_{20,19} = 4 \times 10^{-4} \text{ s}^{-1}$ . Thus, the transitions which have an excitation temperature which is considerably less than the kinetic temperature cover a range in spontaneous decay rates of approximately 50. Naively, one might expect that since the transitions are neither totally unexcited nor thermalized, those with higher spontaneous decay rates would have lower excitation temperatures, as the collisional rates are essentially independent of the rotational quantum number of the initial state.

The quite different behavior that we find is a result of the manner in which the A-coefficients, transition frequencies, and collisional rate coefficients depend on  $J$ . For linear



molecules, a general result is that the excitation temperature is *not* a monotonically decreasing function of  $J$ , despite the fact that the A-coefficients vary as  $J^3$ . Rather,  $T_{ex}$  can be largely independent of  $J$  or even increase with increasing  $J$ , for conditions of relevance in interstellar clouds. This produces the “quasi-thermal” linear curves in Figure 6, with excitation temperatures much less than the kinetic temperature. Collisional cross sections which emphasize transitions in which  $J$  changes by several units enhance this effect. The issue of the dependence of the excitation temperature on  $J$  is discussed further in the Appendix.

## 5.2. Non-*LTE* Excitation and Optical Depth Effects for Linear Molecules

We next consider non-*LTE* effects together with finite optical depths. The combination is significant because the absorption coefficients for the lower  $J$  transitions become larger when the hydrogen density is low, and the molecular population is concentrated in these levels. As shown in Figure 7, the effect is largely what one might expect from the combination of the two separate circumstances. At the lower density,  $n(H_2) = 10^4 \text{ cm}^{-3}$ , considered here, the greatest optical depth occurs for  $5 \leq J_u \leq 9$ , so these transitions are the first to deviate from the quasi-thermal excitation curve as the fractional abundance of  $HC_3N$  is increased. There is a range of  $HC_3N$  fractional abundances per unit velocity gradient, starting at  $X(HC_3N)/dv/dz = 10^{-7} (\text{km s}^{-1}/\text{pc})^{-1}$ , in which the slope of the excitation curve, in the range of transitions lying somewhat above those having maximum optical depth, is increased by the radiative trapping. Thus, the excitation temperature that would be derived from these transitions is enhanced by the trapping. This situation is restricted by the radiative thermalization that is produced when the optical depth reaches a sufficiently high value, with the excitation curve approaching the limiting form determined by black body emission, as discussed in Section 4.4.

## 5.3. Nonlinear Molecules

Non-*LTE* excitation for nonlinear molecules is more complex than for linear species. We again consider E-type methanol as a representative example. We have used the collisional rate coefficients of Peng & Whiteoak (1993), which are not rigorous calculations, but which should be satisfactory for our purpose. Our results do not demand detailed modeling of the behavior of any single transition. Results for three hydrogen densities are shown in Figure 8, for which all transitions are optically thin. The  $CH_3OH$  fractional abundance per unit velocity gradient is  $10^{-14} (\text{km s}^{-1}/\text{pc})^{-1}$ , and we have used a line width of  $1 \text{ km s}^{-1}$  to form the population diagram. This is equivalent to  $N(CH_3OH)/\Delta v =$

$$3.084 \times 10^4 n(\text{H}_2) \text{ (cm}^{-2}/\text{kms}^{-1}\text{)}.$$

For the lowest density of  $10^6 \text{ cm}^{-3}$  we see a clear segregation of the points according to the  $K$ -ladder of the upper level of the transition. The lowest set of points corresponds to  $K = -3$ , the next to  $K = +3$ , and the next to  $K = -2$ . The transitions from states with  $K = +2$ ,  $+1$ , and  $0$  comprise the cluster of points at somewhat higher values of integrated intensity, while the  $K = -1$  transitions fall on a straight line just above this. The levels with different  $J$  for a given value of  $K$  all have the same excitation temperature at each hydrogen density, with  $T_{ex} \simeq 31K$  for  $n_{\text{H}_2} = 10^6 \text{ cm}^{-3}$ ,  $T_{ex} \simeq 45K$  for  $n_{\text{H}_2} = 10^{7.5} \text{ cm}^{-3}$ , and  $T_{ex} = T_k = 50K$  for  $n_{\text{H}_2} = 10^9 \text{ cm}^{-3}$ . The large scatter in the population diagram can thus be an indication of subthermal excitation. Again, however, a large range of transitions must be observed to determine this unambiguously.

## 6. Discussion

In the preceding discussion, we demonstrated that a generalization of the traditional rotation diagram approach improves the capability for analysis of multitransition data to determine excitation temperatures and molecular column densities. Careful consideration of the effects of optical depth and non – *LTE* excitation offer the possibility of improved accuracy, as well as understanding some of the apparently surprising behavior seen in various observational studies. Here we review and comment on some earlier work using the population diagram method, discuss how these results might have to be modified in light of our population diagram analysis, give a specific example, and discuss the effects of clumpiness.

### 6.1. Use of the Population Diagram

Results from the early spectral surveys of Linke, Frerking, & Thaddeus (1979) and Frerking, Linke, & Thaddeus (1979) indicated that populations of a number of levels of several species were described by a single, but very low, excitation temperature. Although we have not analyzed the molecular species observed in these two investigations, we believe that their results can be satisfactorily explained in terms of subthermal excitation in a region of moderately high kinetic temperature, consistent with other information about the Sgr B2 molecular cloud (*cf.* Lis & Goldsmith 1990). Working with a larger data base of molecular lines in the  $3\text{mm}$  wavelength range and using a population diagram analysis Turner (1991) derived both kinetic temperatures and molecular column densities. He also recognized the effect of saturation for some species. While some species could be fit with a single

temperature others required two temperature regimes if one assumed only a linear fit.

There have also been several extensive spectral line surveys at shorter wavelengths used to derive temperatures and densities using the population diagram approach. Serabyn & Weisstein (1995) studied SO, among many other species, and found that analysis of the common  $^{32}\text{SO}$  isotopomer, assuming optically thin emission, required that there be two different temperature components. However, observations of the less abundant  $^{34}\text{SO}$  species indicated that some transitions of  $^{32}\text{SO}$  were optically thick. The analysis of  $^{34}\text{SO}$  was consistent with a single temperature, and allowed these authors to determine the optical depths of transitions of the more abundant species. Adopting this correction, the  $^{32}\text{SO}$  population diagram was consistent with a single temperature of 83 K, reasonably close to the 100 K derived from the  $^{34}\text{SO}$ . This study clearly indicates the significance of optical depth effects, which may be considerably more widespread than can be immediately obvious from observations of a few transitions of a single isotopomer.

Sutton *et al.* (1995) analyzed numerous molecular transitions in the vicinity of the Orion-KL core and found that different species, as well as different isotopomers, gave significantly different temperatures, when analyzed using the rotation diagram approach assuming optically thin *LTE* emission. These variations may be due to a significant extent to the effects of saturation in the more abundant species, and to subthermal excitation as discussed above.

In their study of the disk-outflow system IRAS 20126+4104, Cesaroni *et al.* (1997) analyzed emission from transitions of  $\text{CH}_3\text{CN}$  and  $\text{CH}_3\text{OH}$  using a population diagram approach. In their analysis of the  $\text{CH}_3\text{OH}$   $J = 3 \rightarrow 2$  and  $J = 5 \rightarrow 4$  transitions, these authors adopted a single temperature optically thin fit to derive a rotation temperature of 50 K. However, inspection of their Figure 14 suggests that optical depth effects are likely playing a major role in producing a systematic deviation from the expected linear  $\ln(N_u/g_u)$  versus  $E_u$  relationship. In their analysis of  $\text{CH}_3\text{CN}$  data, a correction for saturation of the ground state lines was applied, which did have the effect of reducing the derived excitation temperature from 260 K to 150 K.

Other uses of the population diagram approach have tended to focus on molecules with complex energy level structures and which hence have many accessible transitions in a limited frequency range. We note in this regard that the results of Blake *et al.* (1994) for  $\text{SO}_2$  are suggestive of saturation producing systematic deviations from optically thin behavior, while the  $\text{CH}_3\text{OH}$  results of van Dishoeck *et al.* (1995) exhibit exactly the kind of scatter seen in Figure 5 here, which is also a consequence of saturation of the stronger lines. Bachiller *et al.* 1995 used  $\text{CH}_3\text{OH}$  to probe the young molecular outflow in L1157, and derived temperatures of 8 K for the ambient gas and 12 K for the outflow. The significance of the temperature difference is probably limited by uncertain effects of saturation, which

the limited data set makes difficult to assess.

These examples suggest that close attention to the effects of saturation and non-*LTE* excitation as discussed here, can only serve to increase our confidence in the molecular column densities and temperatures derived from multi-transition observations.

## 6.2. Analysis of Clumpy Regions

Most of the discussion so far has assumed that the source fills the beam. There are many cases, however, where this is not likely to be the case, and indeed molecular clouds are known to be very clumpy on all scales, with significant chemical inhomogeneities. For example, the early observations on Sgr B2 were made with spatial resolutions on the order of a parsec. It is unlikely that the trace molecules observed by Linke, Frerking, & Thaddeus (1979) and Frerking, Linke, & Thaddeus (1979) fill the volume within the beam size used. If the emission is optically thin or if we can derive the optical depth correction factor, then the only uncertainty in using the population diagram approach is that the column density needs to be scaled upwards by the factor  $[\Delta\Omega_a/\Delta\Omega_s]$ . The problem we face with emission from a clumpy or unresolved region is that the antenna temperatures (or intensities) are reduced by the beam dilution factor (or clump filling factor). Therefore we might detect weak emission with  $T_A \ll T_{kin}$ , and believe that the emission is optically thin. In the case where *LTE* applies, it is a simple matter to modify equation 24 to include a constant offset due to beam dilution,

$$\ln \frac{\gamma_u W}{g_u} = \ln N - \ln \left[ \frac{\Delta\Omega_a}{\Delta\Omega_s} \right] - \ln C_\tau - \ln Z - \frac{E_u}{kT}. \quad (38)$$

As this beam filling factor does not change the shape of the population diagram curves, the analyses discussed above hold here. Independent observations are required to obtain an estimate of the molecular column density in the “filled” region, as distinguished from the beam-averaged column density which is obtained by assuming the dilution factor to be unity.

## 6.3. Application of the Population Diagram for Determination of Molecular Hydrogen Density

The discussion of Section 5 indicates that there is well-defined behavior under non-*LTE* conditions which, in fact, makes the population diagram technique an important one for determination of the density as well as the column density, if we have observations of

transitions that are not thermalized. Together with the more evident ability to diagnose the gas temperature, this means that the population diagram technique can be used as an effective means of tracing two key physical conditions in molecular clouds. Here, we discuss in more detail an example applied to  $CS$  data in two giant molecular cloud cores obtained by Snell *et al.* (1984). This includes observations of the  $2 \rightarrow 1$ ,  $3 \rightarrow 2$ ,  $5 \rightarrow 4$ , and  $6 \rightarrow 5$  transitions, with upper level energies between 7.1 and 49.6  $K$  above the ground state. The Snell *et al.* (1984) data for the central positions of the sources S140 and NGC2024 are plotted in Figure 9.

Several things are immediately evident from the plot. First, the points on the population diagram do fall fairly well on a straight line indicating an excitation temperature of close to 13  $K$ . The transitions appear to be optically thin, which is consistent with conclusions of Mundy *et al.* (1986) based on observation of  $C^{34}S$  in the same sources. The excitation temperature of 13  $K$  is far too low to really be indicative of  $LTE$  in the cores of these GMCs, so we see observational evidence for quasi-thermal excitation discussed in Section 5 and the Appendix. The kinetic temperature in these regions can be determined using a variety of probes, but is likely in the range 30 to 50  $K$ . Model population diagrams for these two kinetic temperatures are shown in the left and right panels of Figure 9, respectively, for  $5.75 \leq \log(n(H_2)/cm^{-3}) \leq 6.5$ . We have adopted a line width of 2  $km\ s^{-1}$  in accordance with the observations, and fixed the  $CS$  column density to be  $N(CS) = 1.09 \times 10^{14}\ cm^{-2}$ .

The population diagram analysis makes quite evident the manner in which the slope of the quasi-thermal excitation curves (inversely proportional to the more-or-less uniform excitation temperature of the transitions considered here) changes as a function of kinetic temperature and hydrogen density. We see a steady decrease in slope (increase in  $T_{ex}$ ) as the hydrogen density increases, and also that a given  $H_2$  density produces a smaller slope (larger excitation temperature) for a higher kinetic temperature. From Figure 9, we see that a density of  $2 \times 10^6\ cm^{-3}$  gives good agreement with the slope of the data points for  $T_k = 30\ K$ , while a density of  $0.6 \times 10^6\ cm^{-3}$  produces a comparably good fit for  $T_k = 50\ K$ . This column density has not been formally “best fit”, but has been chosen to match the data reasonably well. From both panels of the figure we see that  $N(CS)$  would have to be slightly smaller than  $10^{14}\ cm^{-3}$  for both sources.

The analysis by Snell *et al.* (1984) fitted the antenna temperatures directly, treating the  $H_2$  density and  $CS$  column density as independent variables, with the kinetic temperature determined independently. This approach does deal with the data directly, and the extent to which the model and the data agree or disagree is clearly evident. The results of the fitting by Snell *et al.* (1984) and those given here above are quite consistent. We do not feel that there should, in fact, be any systematic differences between the two approaches.

The population diagram approach offers the following quite clear advantages:

1. There is the possibility of recognizing optical depth effects directly from the form of the data, although this will, in general, require quite a large number of transitions spread over a range of upper state energies.
2. The appearance of quasi-thermal excitation immediately gives an independent lower limit to the kinetic temperature.
3. The trade-off between kinetic temperature and hydrogen density is quite evident, which is not at all the case when fitting unprocessed data directly.
4. If one can demonstrate that *LTE* does apply, then the kinetic temperature and the total molecular column density can be immediately obtained with good accuracy.
5. The ability to recognize the presence of multiple temperatures is a potential advantage, but needs to be approached with caution in view of the concerns raised earlier about excitation and optical depth effects.

The population diagram and direct analysis methods both have the quality of being able to separate the effect of column density and space density changes. In view of its advantages and lack of any apparent drawbacks, there does not appear to be any reason not to use the population diagram approach for determination of physical conditions in dense clouds from multi-transition molecular line data.

## 7. Summary

We have examined in some detail the “rotation diagram” for analysis of multi-transition molecular emission data, which we feel is better called the “population diagram” technique. In this approach, the natural logarithm of the integrated intensity of each transition observed, multiplied by appropriate constants, is plotted against the energy of the upper level of the transition. The traditional use of this type of diagram has been to assume that the emission is optically thin, and that *LTE* applies. In this limiting case, the integrated intensity is proportional to the upper level column density, and the column densities are related by Boltzmann factors, so that the locus of points on the population diagram should be a straight line, with slope proportional to the negative reciprocal of the temperature. A straightforward generalization of this technique to include the optical depth  $\tau$ , and optical depth correction factor  $C_\tau = \frac{\tau}{1-e^{-\tau}}$ , but still assuming populations of all levels are in *LTE* at temperature  $T$ , gives the relationship

$$\ln \frac{\gamma_u W}{g_u} = \ln N - \ln C_\tau - \ln Z - \frac{E_u}{kT}, \quad (39)$$

where  $\gamma_u$  is the combination of constants relating integrated line intensity and upper level column density,  $N$  is the total molecular population,  $Z$  is the partition function, and  $E_u$  the upper state energy. We have derived the correction factor for linear molecules in *LTE* in analytic form, and have used  $\text{CH}_3\text{OH}$  as representative of more complex molecules, to show how saturation can produce both systematic and apparently “scatter-like” deviations from optically thin behavior. These effects have been recognized to various degrees in papers in the literature, and we suggest that a more systematic approach to consideration of saturation effects could improve reliability of molecular column density and temperature determinations.

We have examined the non-*LTE* behavior of linear molecules, and have found that the apparent constancy of excitation temperature among levels with quite different spontaneous decay rates can be understood in terms of the frequency dependence of the quantities involved. This quasi-thermalization at excitation temperatures well below the kinetic temperature explains apparently surprising results reported in the literature. We have also examined the population diagram as a technique to determine molecular hydrogen densities, which involves comparison of the form of the population diagram curves with statistical equilibrium/radiative transfer code predictions. This approach appears to offer several important advantages compared to fitting intensities directly, including recognition of *LTE*, bounding the kinetic temperature, and clearly indicating the interrelated effects of the kinetic temperature and the excitation rate.

The National Astronomy and Ionosphere Center is operated by Cornell University under a cooperative agreement with the National Science Foundation. The research of WDL was conducted at the Jet Propulsion Laboratory, California Institute of Technology, with support from NASA research grants.

## APPENDIX

### Quasi-Thermal Excitation

The curious behavior of the relative intensities, and hence the level populations of linear molecules discussed in Sections 5.1 and 6.3 deserves some further comment beyond that appropriate for the main text. The result suggested by Figure 6 is that the excitation temperature can remain relatively constant, or even increase as the rotational quantum number  $J$  increases. This behavior is surprising because we know from equation 25 that the A-coefficients increase rapidly with increasing  $J$ , so that in the case of subthermal excitation, we might think that the higher transitions are further from thermalization, and hence their excitation temperatures should be lower. This proves not necessarily to be the case, however.

We can gain valuable insight into this question by examining initially a simplified version of the problem, which is just to consider a two level system. However, it should be borne in mind that this is also directly applicable to the case of a linear molecule provided that the collisions connect only adjacent levels, *e.g.* are "dipole collisions". This behavior is not a precise description for most molecular species interacting with neutral collision partners, but the behavior that is found shows the same basic characteristics as that obtained from multilevel statistical equilibrium calculations using computed collision rates which allow collisions with a range of  $\Delta J$ .

In the case of dipole collisions, as discussed by Goldsmith (1972), the relative populations of each pair of levels is decoupled from that of other levels. If we neglect the background radiation field, we obtain from the rate equations that the excitation temperature is given by the expression

$$T_{ex} = \frac{h\nu/k}{h\nu/kT_k + \ln(1 + A_{ul}/C_{ul})} . \quad (1)$$

Defining

$$\chi = \frac{A_{ul}}{C_{ul}} \quad (2)$$

and

$$K = \frac{h\nu}{kT_k} , \quad (3)$$

we obtain the simple and convenient expression

$$\frac{T_{ex}}{T_k} = [1 + \frac{1}{K} \ln(1 + \chi)]^{-1} . \quad (4)$$



$\chi$  and  $K$  can be considered independent variables that determine the  $T_{ex}$  as a fraction of  $T_k$ . The relationship is shown in Figure A1, in which the different sets of points correspond to different values of  $K$ , as a function of  $\chi$ . We see that for a given value of  $K$ ,  $T_{ex}$  as a fraction of  $T_k$  increases monotonically as  $\chi$  drops, which corresponds to moving closer to thermalization as the ratio of the collision rate to the spontaneous decay rate increases. For a fixed value of  $\chi$ ,  $T_{ex}/T_k$  increases as  $K$  increases. Thus, for a fixed ratio of spontaneous decay rate to collisional deexcitation rate, as the transition frequency relative to the kinetic temperature (both expressed as energies) increases, the excitation temperature relative to the kinetic temperature also increases. If we consider a fixed kinetic temperature, as the transition frequency increases,  $K$  increases, and thus so does the excitation temperature.

This really reflects the definition of the excitation temperature in terms of a Boltzmann factor relating the upper and lower level populations (*cf.* equation 18). A fixed kinetic temperature and  $\chi$  mean a fixed ratio of upwards to downwards transition rates, which from the basic definition of the rate equation translates to a fixed ratio of transition frequency to excitation temperature. Thus a greater transition frequency requires a higher excitation temperature to achieve the same ratio of level populations, and *vice-versa*.

If we consider the situation with the transition frequency fixed, as the kinetic temperature is increased,  $K$  decreases, but the fact that  $T_{ex}/T_k$  rises in consequence does not immediately indicate what happens to the excitation temperature itself. If we consider the limit  $h\nu \ll kT_k$ , for  $\chi$  not too small (*i.e.* if we are not too close to *LTE*), equation 4 becomes

$$T_{ex} = \frac{h\nu/k}{\ln(1 + \chi)} . \quad (5)$$

We see that in this limit, the excitation temperature is independent of the kinetic temperature. Thus the sets of points for different values of  $\log K$  at a fixed  $\chi$ , which are separated by 0.5 dex, give values of  $\log(T_{ex}/T_k)$  which differ by this same factor.

The situation for a linear molecule with a “ladder” of transitions is somewhat more involved. As the frequency and spontaneous decay rate both depend on the transition in question,  $K$  and  $\chi$  are not independent variables. Knowing the variation of frequency and spontaneous decay rate as a function of  $J$ , it is possible to see how the various transitions of a linear molecule are located in Figure A1. It is more convenient, however, to express  $K$  and  $\chi$  in terms of parameters that characterize the  $J = 1 \rightarrow 0$  transition, through

$$K = K_1 J , \quad (6)$$

and

$$\chi = \chi_1 \frac{3J^4}{2J+1}, \quad (7)$$

where

$$K_1 = \frac{h\nu_{10}}{kT_k}, \quad (8)$$

and

$$\chi_1 = \frac{C_{10}}{A_{10}}. \quad (9)$$

We assume that all transitions are characterized by equal deexcitation rates, which is reasonably close to what is found from realistic calculations of cross sections.

The calculation of the excitation temperature as a function of  $K_1$ ,  $\chi_1$ , and  $J$  is shown in Figure A2. We now see something quite different as we move up the rotational “ladder” – for a wide range of conditions  $T_{ex}/T_k$  is essentially independent of  $J$ . Note in particular that even for modest values of  $K$  between 0.01 and 0.10, the quasi-independence of excitation temperature of  $J$  starts at quite modest values of  $J$ , between 5 and 10. As an example, *CS* at a kinetic temperature of 23 K corresponds to  $K_1 = 0.1$ , and we see that transitions for  $J$  greater than a few are predicted to have an excitation temperature of about 10 K for  $\chi_1 = 0.1$ . Taking a collision rate coefficient of  $2 \times 10^{-11} \text{ cm}^3 \text{ s}^{-1}$ , we find that this corresponds to a density of  $10^3 \text{ cm}^{-3}$ . In a basic sense, dipole collisions can produce excitation temperatures that are largely independent of  $J$ .

The quasi-thermal behavior with  $T_{ex} < T_k$  is emphasized by the form of the actual collision cross sections. This point is addressed in Figure A3, which compares the population diagrams obtained for the standard “hard” collisions with those from “dipole” collisions. These calculations were carried out including the 2.7 K background radiation field. The abundance of *HC<sub>3</sub>N* is sufficiently low that all transitions are optically thin. The deexcitation rates from Green & Chapman (1978) allow  $-10 \leq \Delta J \leq 0$  with significant probability, and  $-20 \leq \Delta J \leq 0$  with non-zero probability. For dipole collisions, we restrict the nonzero deexcitation rates to transitions with  $\Delta J = -1$ , but multiply these rates by a scaling factor such that the deexcitation rate is the same as the total deexcitation rate for hard collisions. This factor is found to be approximately 2.4 for initial  $J$  greater than a few, and closer to unity for smaller initial  $J$ . We see for the dipole collisions that there is significantly lower excitation of the higher- $J$  levels. For  $n(H_2) = 10^3 \text{ cm}^{-3}$ , the excitation temperature is 2.7 K (close to the background temperature), compared to 5 K for the hard collisions. For  $n(H_2) = 10^4 \text{ cm}^{-3}$ , the excitation temperatures produced by the scaled

dipole collisions are about  $3.3\text{ K}$ , compared to  $8\text{ K}$  for the hard collisions. For densities in excess of  $10^7\text{ cm}^{-3}$  all transitions are thermalized for scaled dipole collisions. Thus, the collisions which produce a large change in  $J$  result in values of  $T_{ex}$  that are significantly above the background temperature and are also essentially independent of  $J$ .

## REFERENCES

- Bachiller, R., Liechti, S., Walmsley, C.M., & Colomer, F. 1995, *A&A*, 295, L51
- Blake, G.A., van Dishoeck, E.F., Jansen, D.J., Groesbeck, T.D., & Mundy, L.G. 1994, *ApJ*, 428, 680
- Cesaroni, R., Fell, M., Testi, L., Walmsley, C.M., & Olmi, L. 1997, *A&A*, 325, 725
- Frerking, M.A., Linke, R.A., & Thaddeus, P. 1979, *ApJ*, 234, L143
- Goldsmith, P.F. 1972, *ApJ*, 176, 597
- Green, S. & Chapman, S. 1978, *ApJS*, 37, 169
- Kraus, J.D. 1966, *Radio Astronomy* (New York, NY: McGraw-Hill), p. 157.
- Lis, D.C. & Goldsmith, P.F. 1990, *ApJ*, 356, 195
- Lafferty, W.J. & Lovas, F.J. 1978. *J. Phys. Chem. Ref. Data*, 7, 441
- Linke, R.A., Frerking, M.A., & Thaddeus, P. 1979, *ApJ*, 234, L139
- Mundy, L.G., Snell, R.L, Evans, N.J. II, Goldsmith, P.F., & Bally, J. 1986, *ApJ*, 306, 670
- Peng, R.S. & Whiteoak, J.B. 1993, *MNRAS*, 260, 529
- Serabyn, E. & Weisstein, E.W. 1995, *ApJ*, 451, 238
- Snell, R.L., Mundy, L.G., Goldsmith, P.F., Evans, N.J. II, & Erickson, N.R. 1984, *ApJ*, 276, 625
- Sutton, E.C., Peng, R., Danchi, W.C., Jaminet, P.A., Sandell, G., & Russell, A.P.G. 1995, *ApJS*, 97, 455
- Turner, B.E. 1991, *ApJS*, 76, 617
- van Dishoeck, E.F., Blake, G.A., Jansen, D., & Groesbeck, T.D. 1995, *ApJ*, 447, 760
- Wilson, T.L., Henkel, C., Hüttemeister, S., Dahmen, G., Linhart, A., Lemme, C., & Schmidt-Burgk, J. 1993, *A&A*, 276, L29

Fig. 1.— Variation of relative optical depth of rigid rotor transitions in *LTE* as a function of  $J$  for different values of the rotation constant relative to the kinetic temperature.

Fig. 2.— Population diagrams for  $HC_3N$ . The  $H_2$  density of  $10^9 \text{ cm}^{-3}$  ensures that all transitions are thermalized, so that *LTE* applies. At the kinetic temperature of 22 K,  $a = hB_0/kT = 0.01$ . The curves correspond to different fractional abundances per unit velocity gradient as indicated by the symbols shown in the lower left. The maximum optical depth for  $X = 10^{-11}$  is 377, which occurs for the  $J = 10 \rightarrow 9$  transition. The corresponding optical depth of the  $1 \rightarrow 0$  transition is 10, and for the  $18 \rightarrow 17$  transition is 130. The optical depths scale directly with the fractional abundance.

Fig. 3.— Optical depth correction factor as a function of upper level energy for different values of the opacity of the  $HC_3N$   $1 \rightarrow 0$  transition. The value of  $a = hB_0/kT$  is indicated in each panel. The circles are for  $\tau_{1,0} = 0.001$ , the squares for  $\tau_{1,0} = 0.01$ , and the triangles for  $\tau_{1,0} = 0.1$ . The negative of the natural logarithm of  $C_\tau$  is plotted so that the resulting curves have the same orientation as the effect of the finite optical depth on the population diagram.

Fig. 4.— Energy levels below  $E/k = 160K$  with  $|K| \leq 3$  for E-type methanol with quantum numbers  $J$  and  $K$  indicated. We show the radiative transitions that involve the (8,2) level. There are five transitions *into* this level (indicated by dashed lines); three with  $\Delta K = +1$ , one with  $\Delta K = 0$ , and one with  $\Delta K = -1$ . There are three transitions *out of* the (8,2) level (indicated by dotted lines), one with  $\Delta K = 0$ , and two having  $\Delta K = +1$ .

Fig. 5.— Population diagrams for E-type methanol based on levels below  $E/k = 160K$  having  $|K| \leq 3$ . We take a velocity gradient equal to  $1 \text{ kms}^{-1}/pc$ , so that the fractional abundances per unit velocity gradient indicated in the lower left correspond to the fractional abundances of  $CH_3OH$ . For the lower  $CH_3OH$  fractional abundances, there are generally more than one optically thin transition from a given upper level, which all appear as a single point. As the fractional abundance increases, the transitions with larger optical depth fall below those extrapolated from optically thin results. For  $X(CH_3OH) = 10^{-11}$ , there are transitions with  $\tau$  as low as 0.25, and as large as 30, which produces the apparent scatter in the upper level column densities derived without correction for the finite optical depths.

Fig. 6.— Population diagrams for  $HC_3N$  levels up to 70  $K$  above the ground state (including  $J = 0$  to  $J = 18$ ). The fractional abundance of  $HC_3N$  per unit velocity gradient is chosen to make all transitions optically thin for all hydrogen densities considered, which vary from  $10^3 \text{ cm}^{-3}$  to  $10^8 \text{ cm}^{-3}$  as indicated by the symbols shown at lower left of figure. For hydrogen densities  $n(H_2) \geq 10^7 \text{ cm}^{-3}$ , all transitions are thermalized and the population diagram curves are straight lines characteristic of the kinetic temperature of 22  $K$ . For lower densities, a variety of effects are seen, including quasi-thermalization at a temperature considerably less than the kinetic temperature.

Fig. 7.— Effect of finite optical depth on subthermally excited  $HC_3N$ . The curves are for different molecular fractional abundances. A velocity gradient of  $1 \text{ kms}^{-1}/pc$  has been used to form the population diagrams. The integrated intensity is limited by the optically thick  $LTE$  curve defined by the diamond symbols. The maximum values of the optical depth for collisional excitation alone are in the region  $5 \leq J_u \leq 9$ , while for  $LTE$ , the optical depth distribution is much more widely distributed and peaks at  $J_u = 11$ .

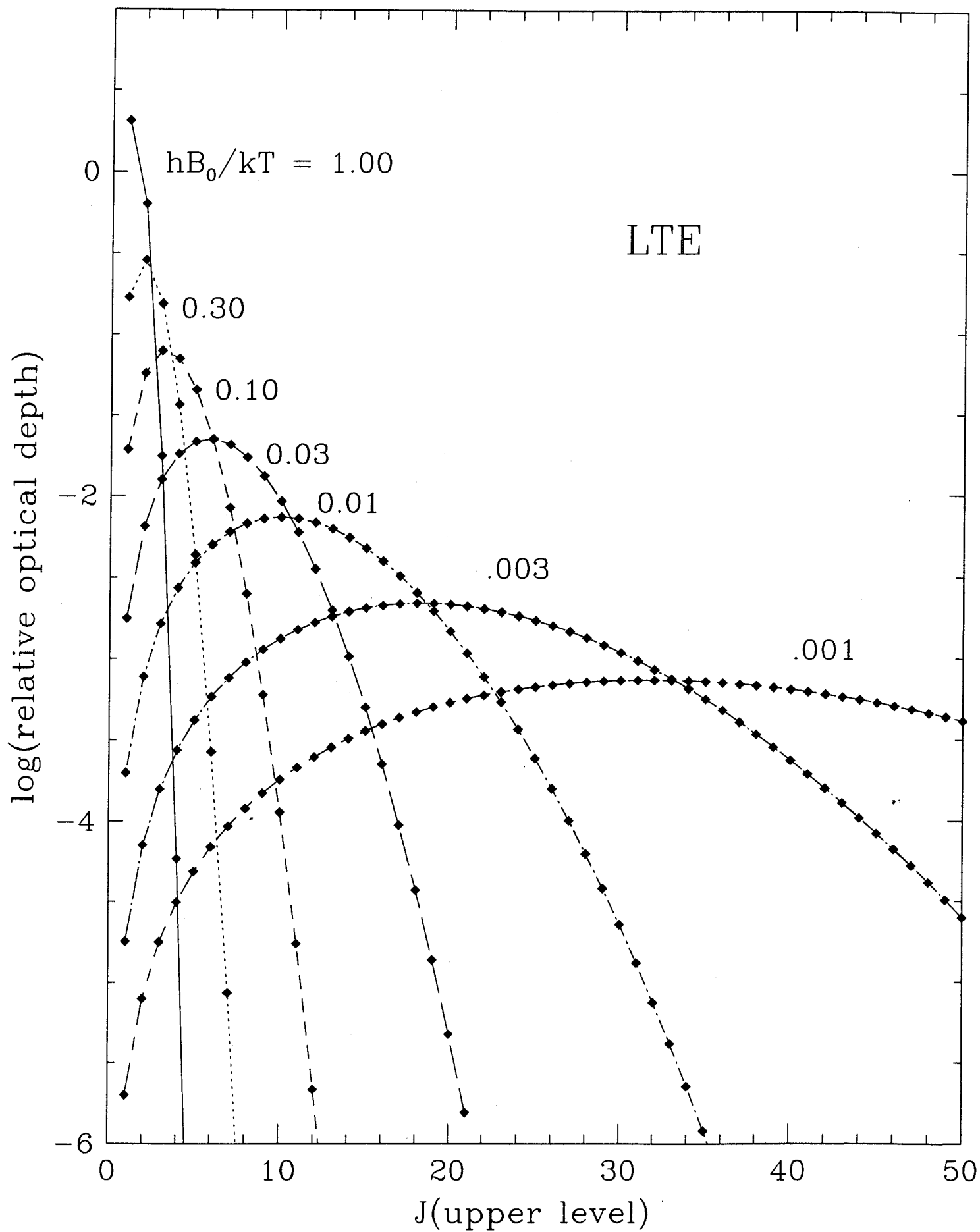
Fig. 8.— Population diagrams for optically thin  $CH_3OH$  at hydrogen densities of  $10^6$ ,  $10^{7.5}$ , and  $10^9 \text{ cm}^{-3}$ . The fractional abundance per unit velocity gradient of  $CH_3OH$  is  $10^{-14}(\text{kms}^{-1}/pc)^{-1}$  and a velocity gradient of  $1 \text{ kms}^{-1}/pc$  has been used to construct the population diagrams. For the lowest hydrogen density, the upper levels from different  $K$  ladders are relatively distinct, with the lowest group being the transitions in the  $K = -3$  ladder, the next group the transitions in the  $K = +3$  ladder, then those in the  $K = -2$  ladder, while the highest group includes transitions in the remaining ladders. At a density of  $10^{7.5} \text{ cm}^{-3}$ , only the levels from the  $K = -3$  ladder are significantly below the  $LTE$  curve, while for the highest  $H_2$  density, all transitions considered here are essentially thermalized.

Fig. 9.— Population diagram analysis of multi-transition  $CS$  data from Snell *et al.* 1984. Data from the (0,0) position in sources S140 and NGC 2024 are plotted as large triangles and filled squares, respectively, while the results from different  $H_2$  densities are indicated by symbols as defined in r.h. panel. The slope of the population diagram for  $LTE$  at 13  $K$  is indicated by the heavy curve in lower l.h. panel. The results of model calculations at a kinetic temperature of 30  $K$  are shown in the l.h. panel, and for 50  $K$  in the r.h. panel. We have adopted a line width of  $2 \text{ kms}^{-1}$  in accordance with the observations, and the  $CS$  column density is  $1.09 \times 10^{14} \text{ cm}^{-2}$  for all of the curves.

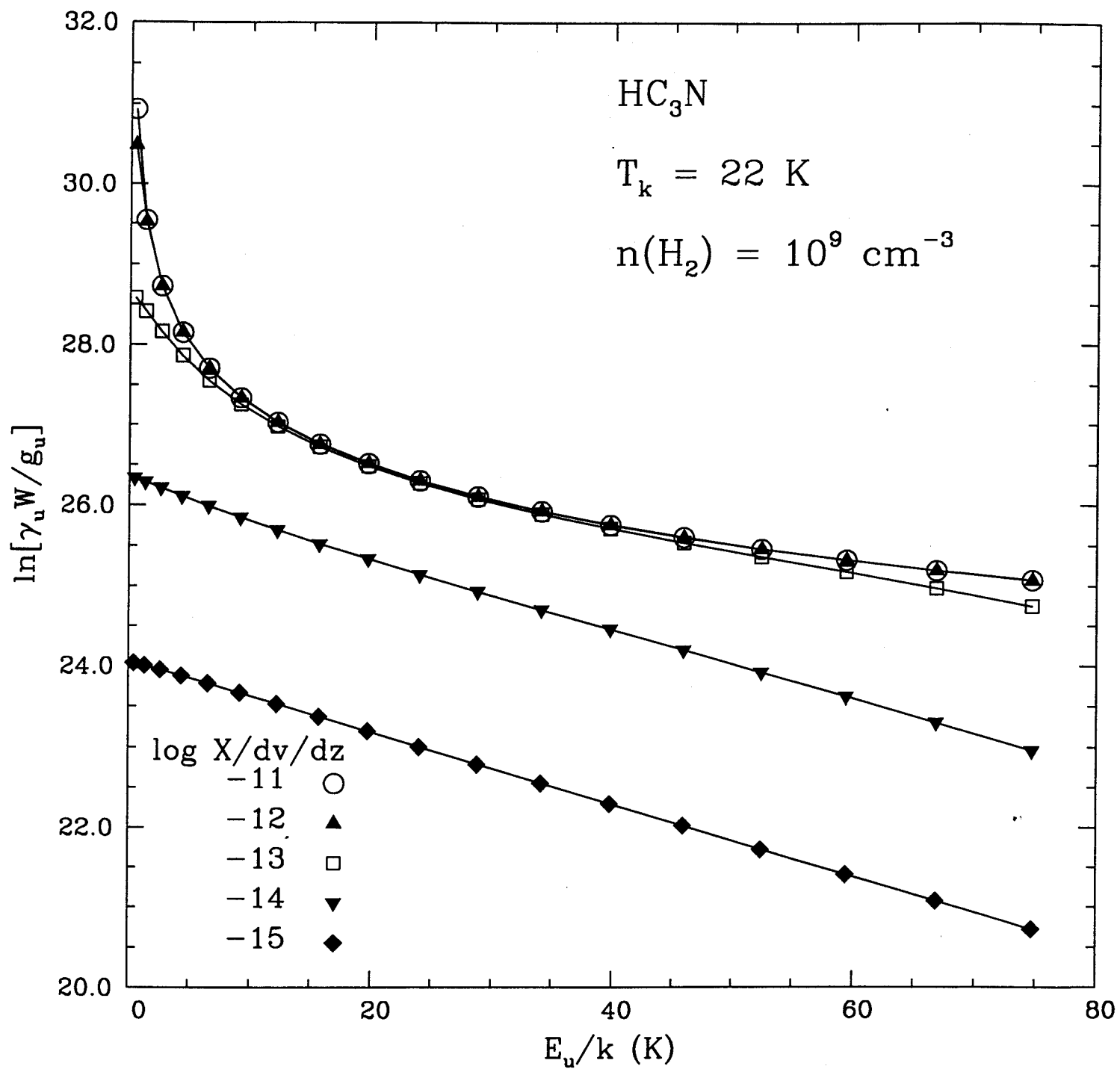
Fig. 10.— Solution of two level system in which the excitation temperature relative to the kinetic temperature is calculated as a function of the parameters  $\chi = A_{ul}/C_{ul}$ , the ratio of spontaneous to collisional deexcitation rates, and  $K = E_{ul}/kT_k$ , the ratio of the energy difference of the transition to the energy corresponding to the kinetic temperature. There is no background radiation considered in this calculation, which also assumes the transition is optically thin.

Fig. 11.— Excitation temperature for different transitions of a linear molecule with collisional excitation by dipole collisions ( $\Delta J = \pm 1$ ). The parameters  $\chi_1$  and  $K_1$  apply to the  $1 \rightarrow 0$  transition and define the ratios of the spontaneous to collisional deexcitation rate and the energy of the transition to that of the kinetic temperature, respectively. For significant ranges of  $J$  as well as of the parameters defining the conditions in which the molecules are found, the excitation temperature is essentially independent of  $J$ .

Fig. 12.— Comparison of population diagrams for  $HC_3N$  assuming different excitation models. The solid curves are for “hard” collisions, which reflect realistic intermolecular forces and which allow changes in the rotational quantum number to take place with substantial probability for  $\Delta J$  up to 10. The dotted curves are for dipole collisions, in which  $\Delta J = \pm 1$ . The hard collisions produce significantly greater excitation of the higher  $J$  transitions for hydrogen densities  $\leq 10^5 \text{ cm}^{-3}$  than do the dipole collisions. The conditions are otherwise the same as described for Figure 6.







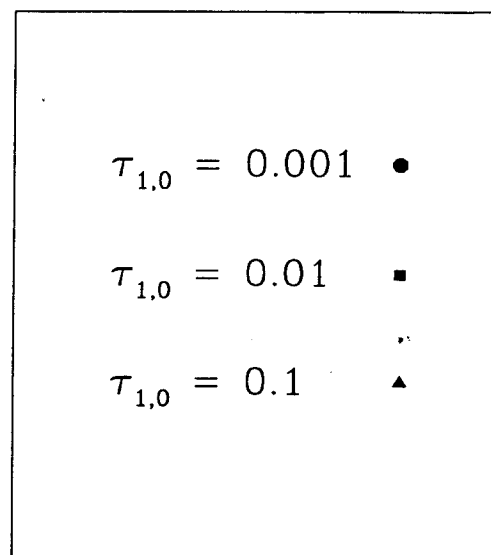
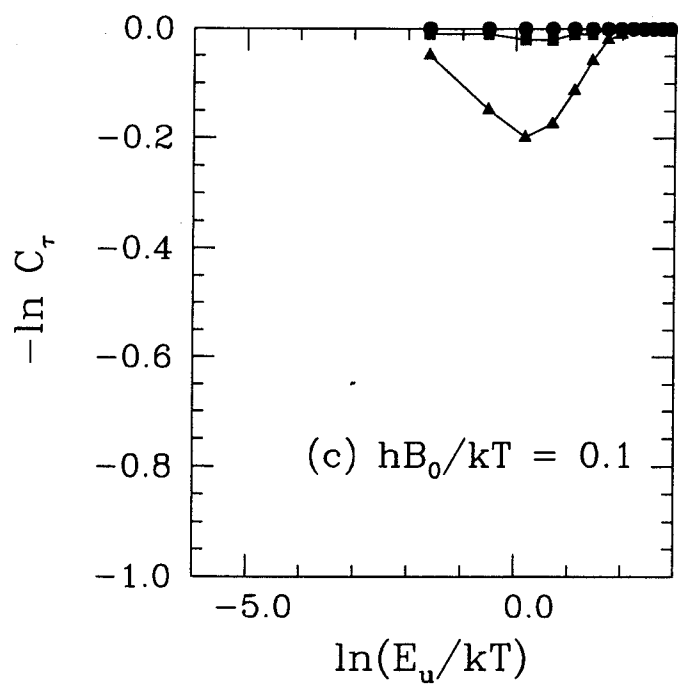
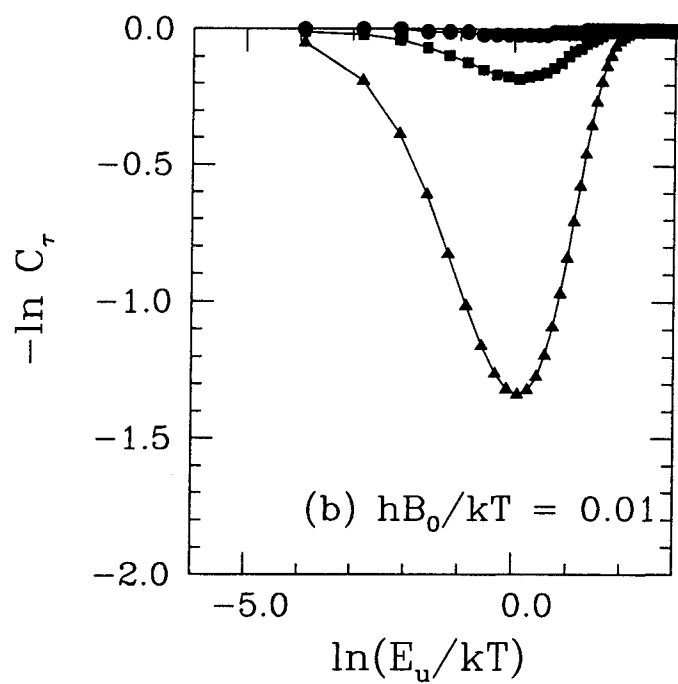
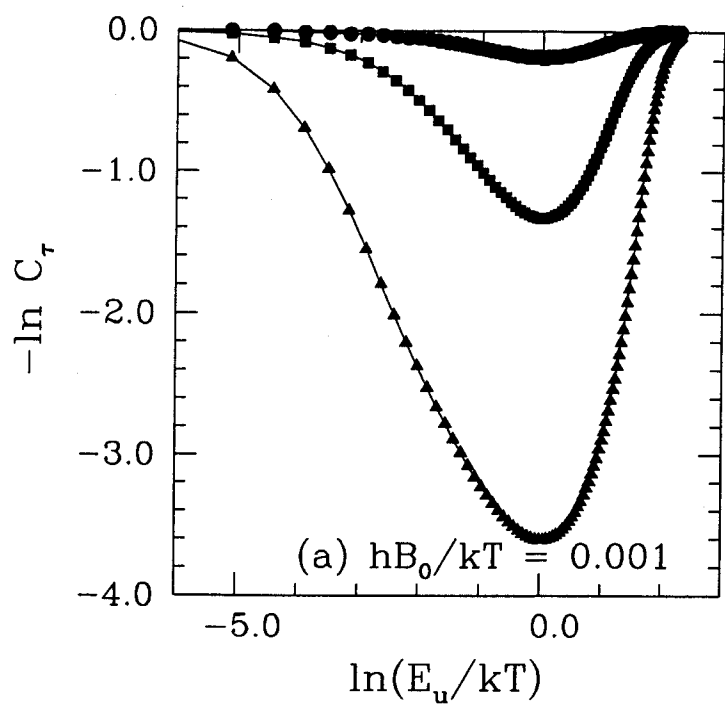


Fig 3

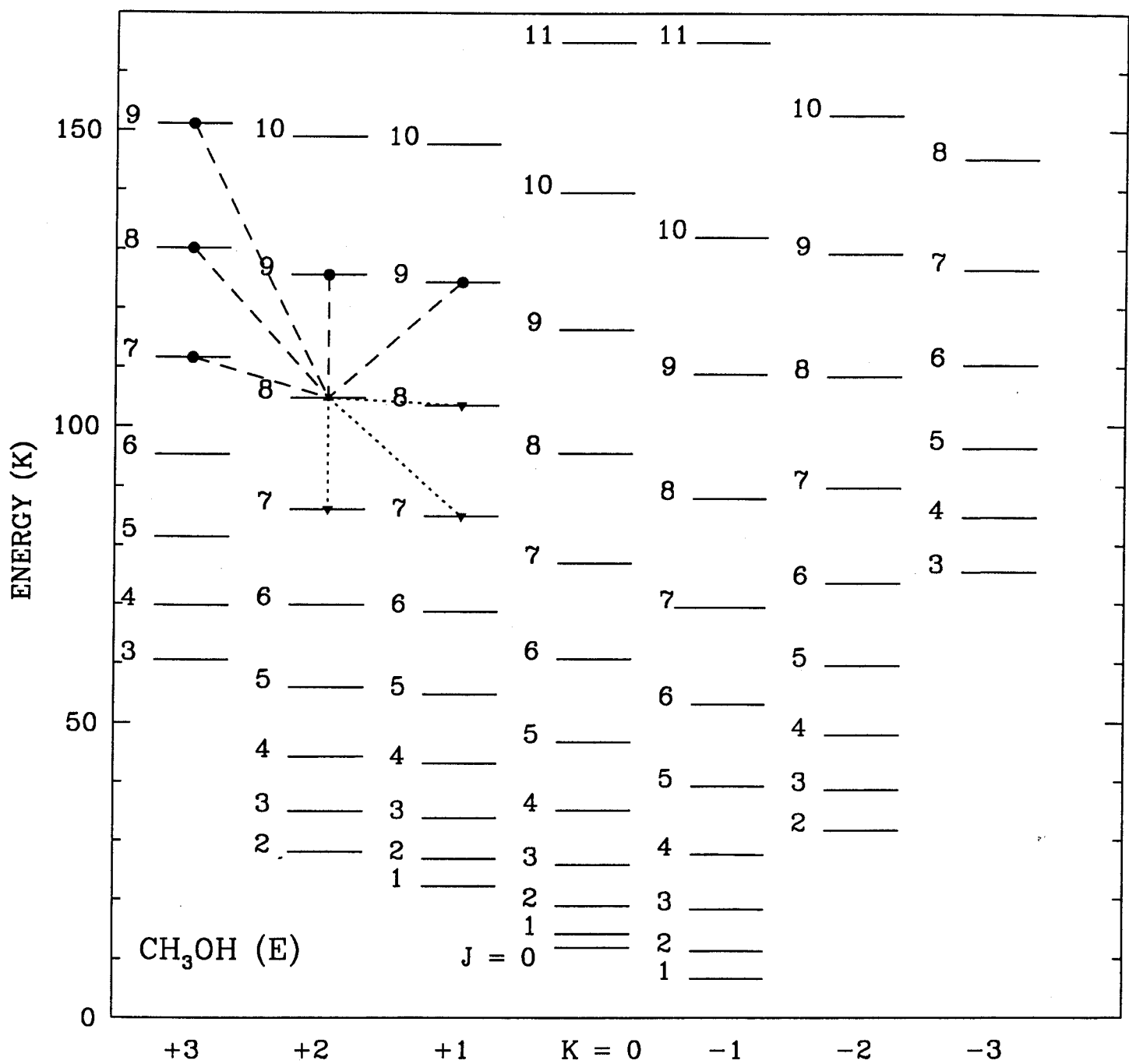


Fig 4

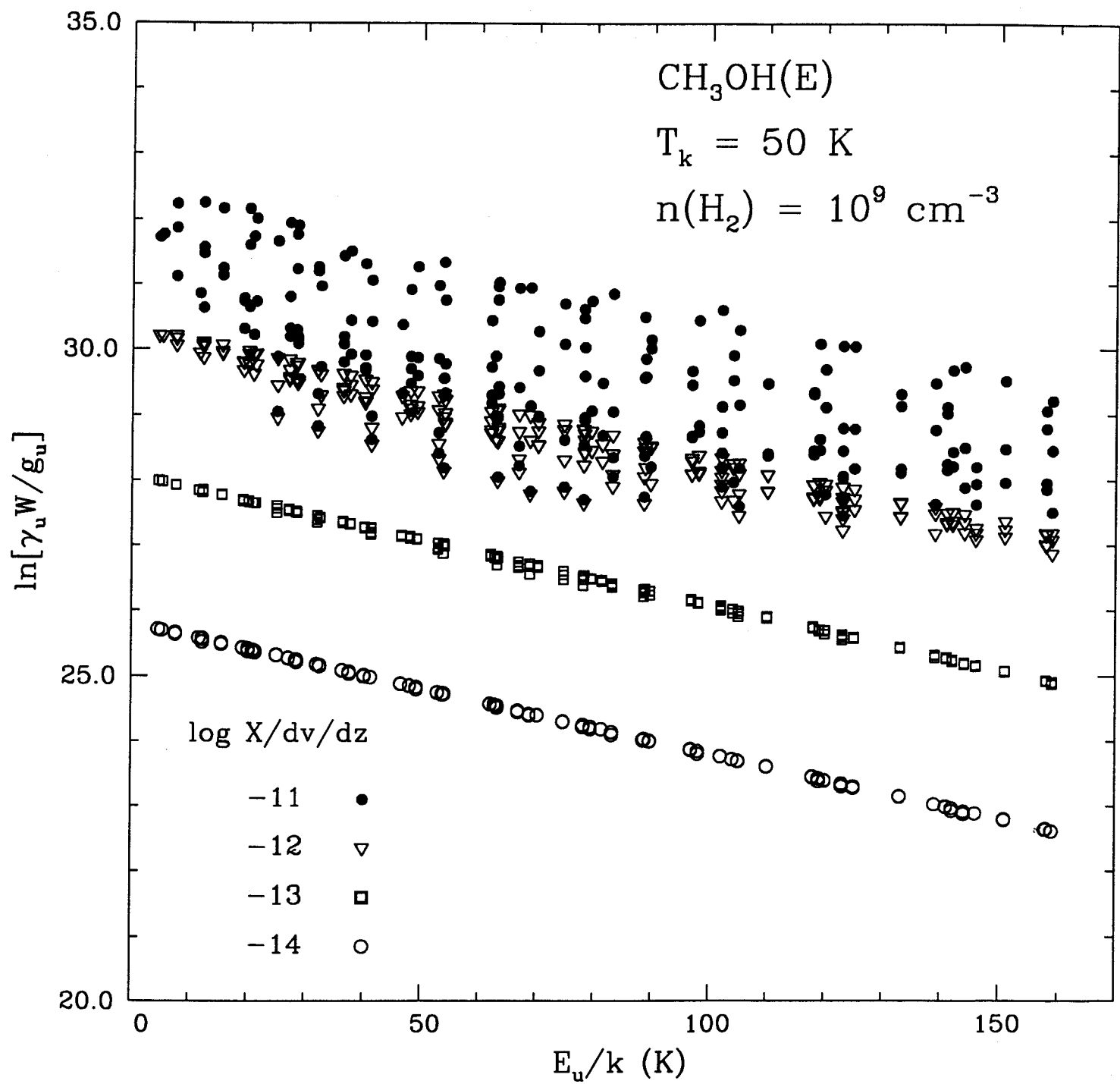


Fig 5

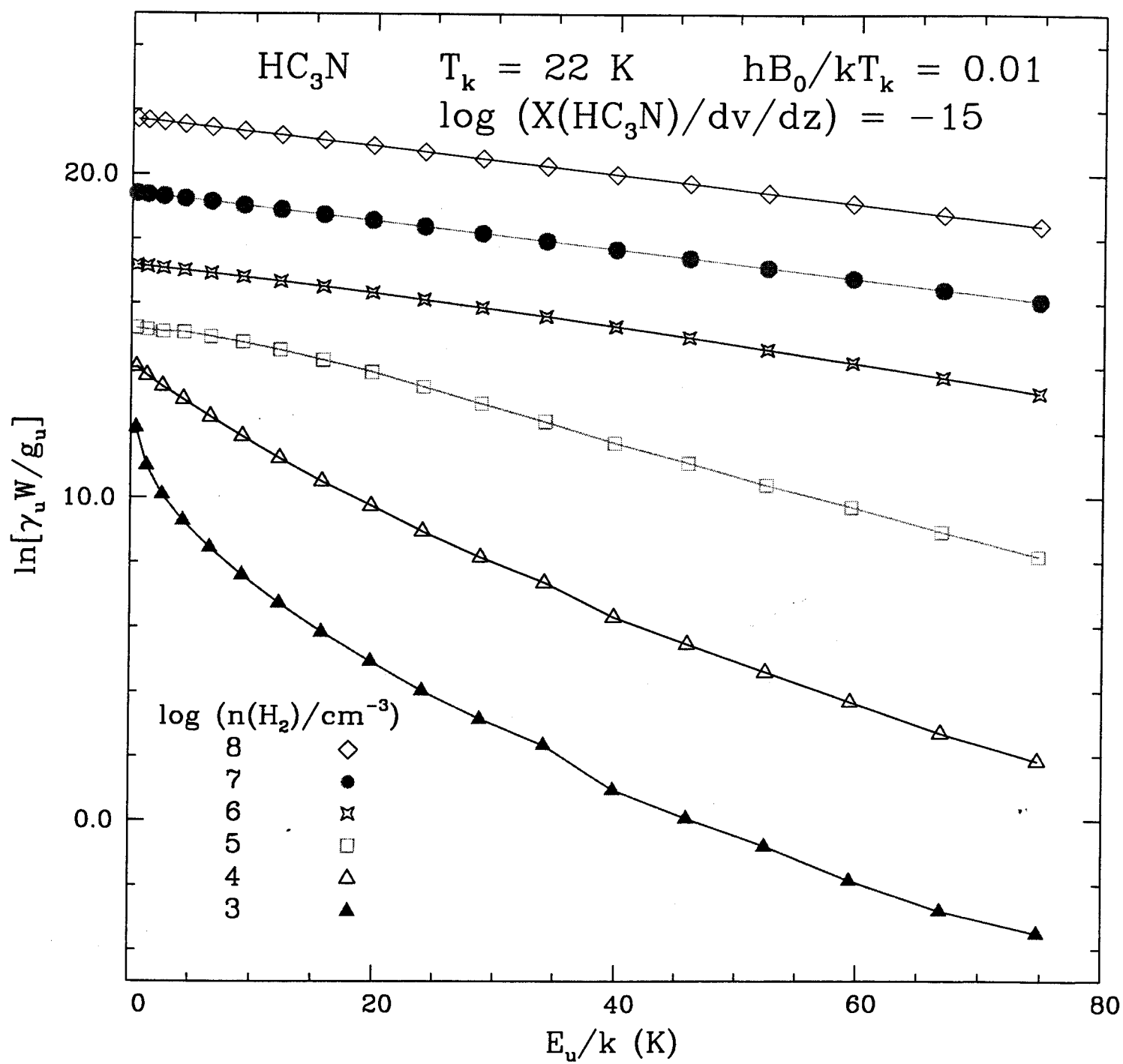
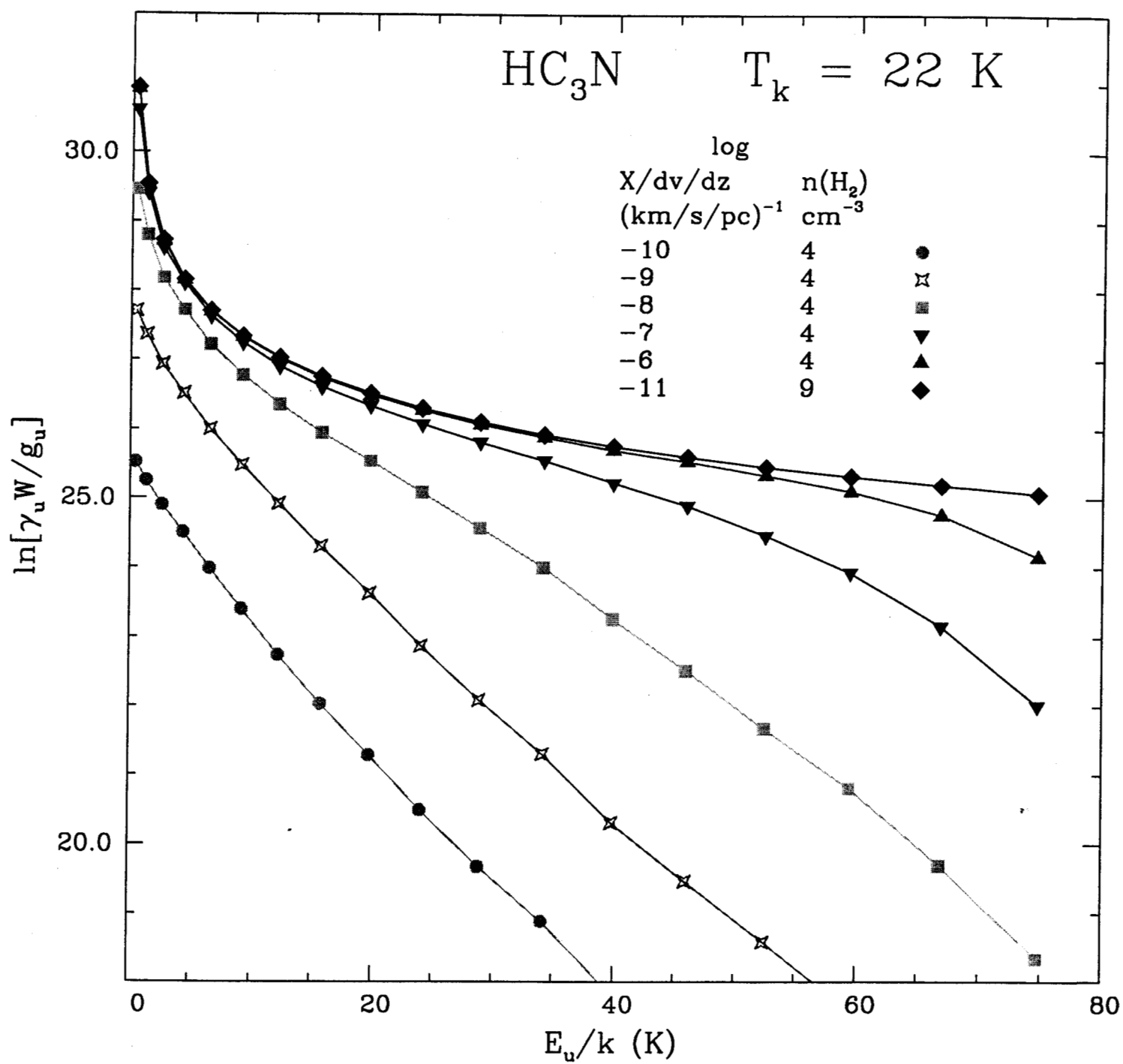


Fig 6



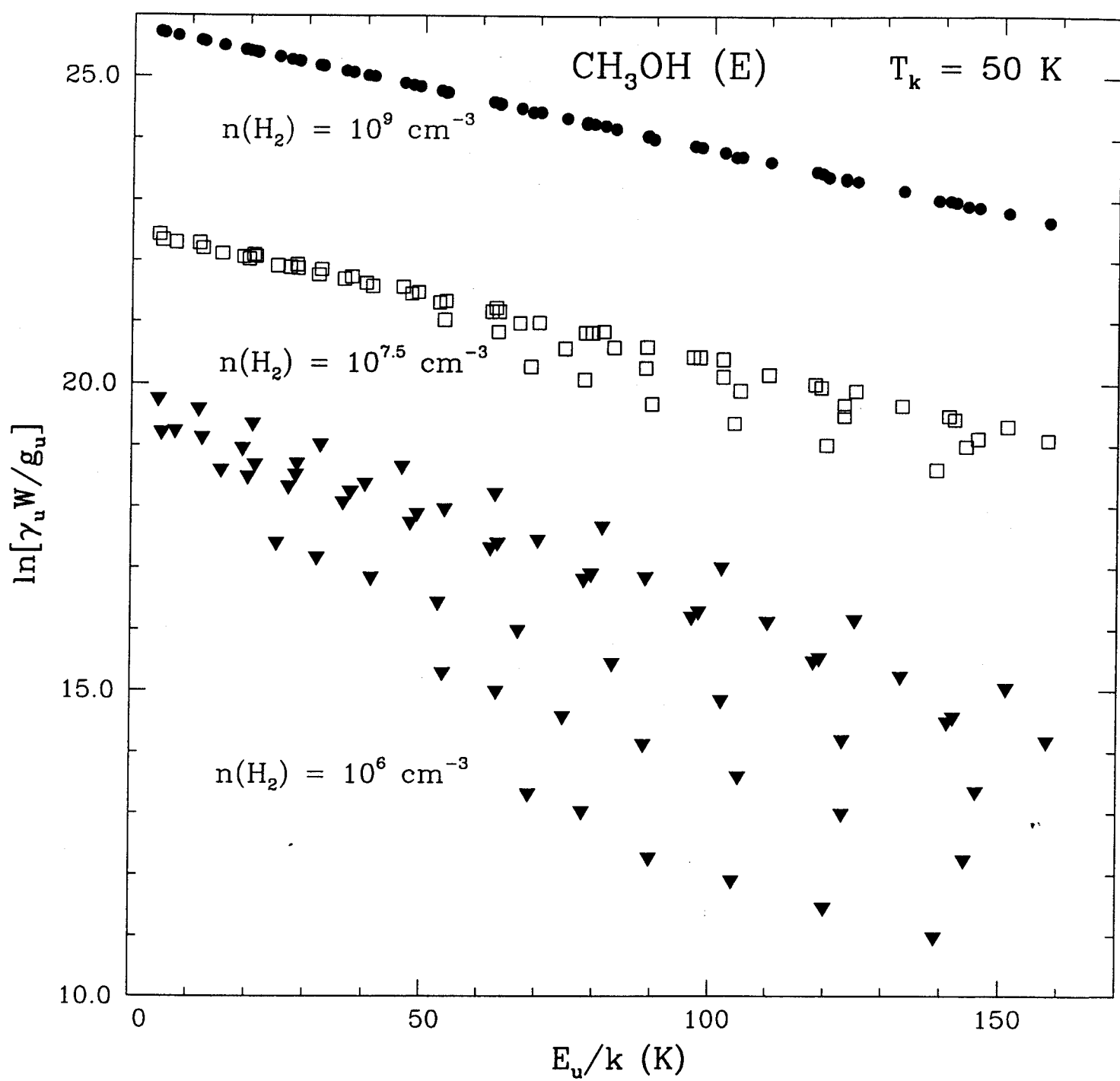


Fig 8

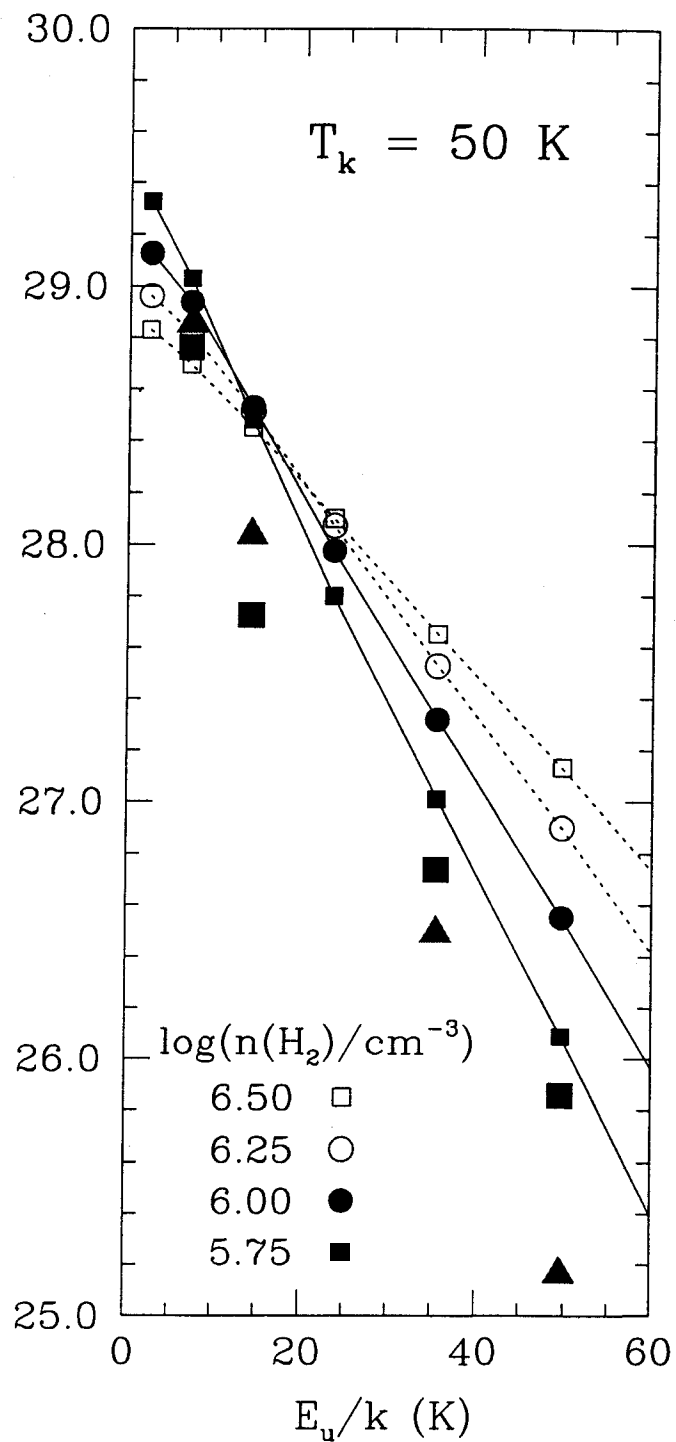
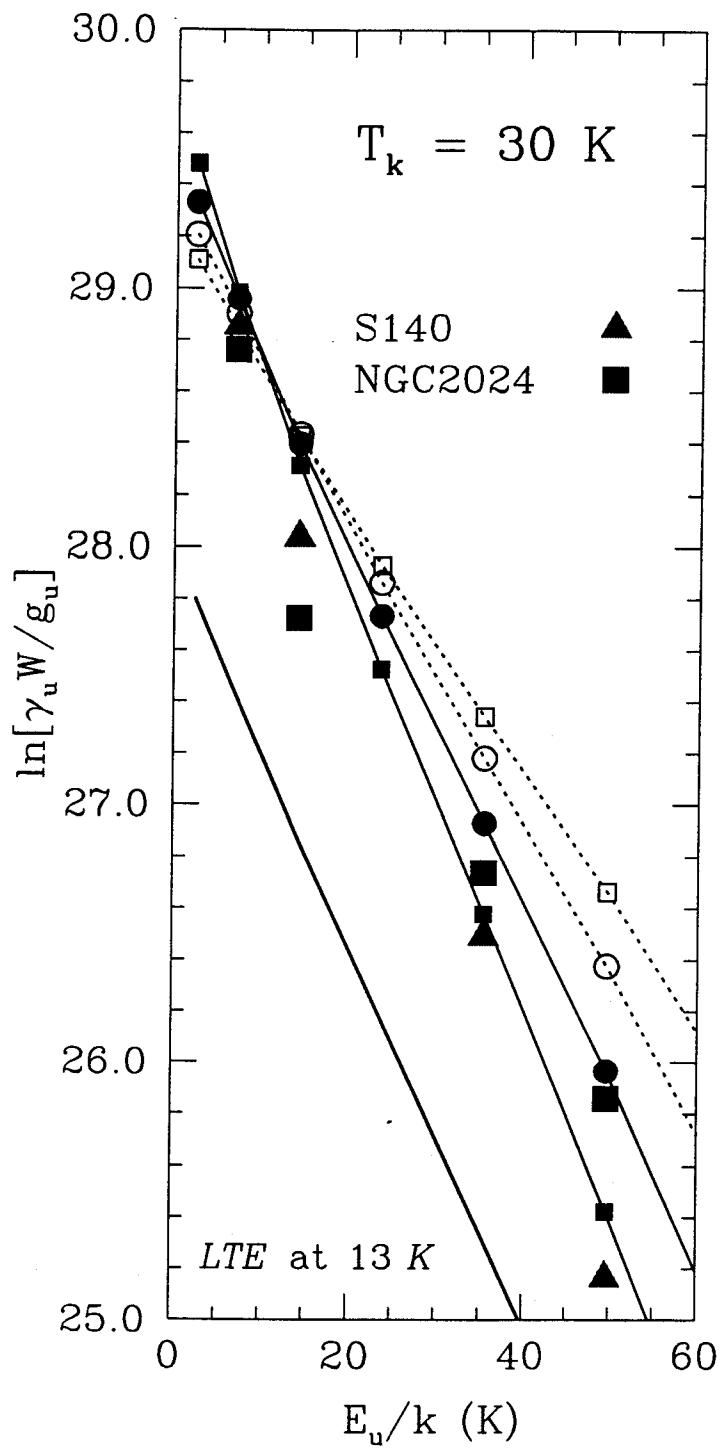


Fig 9



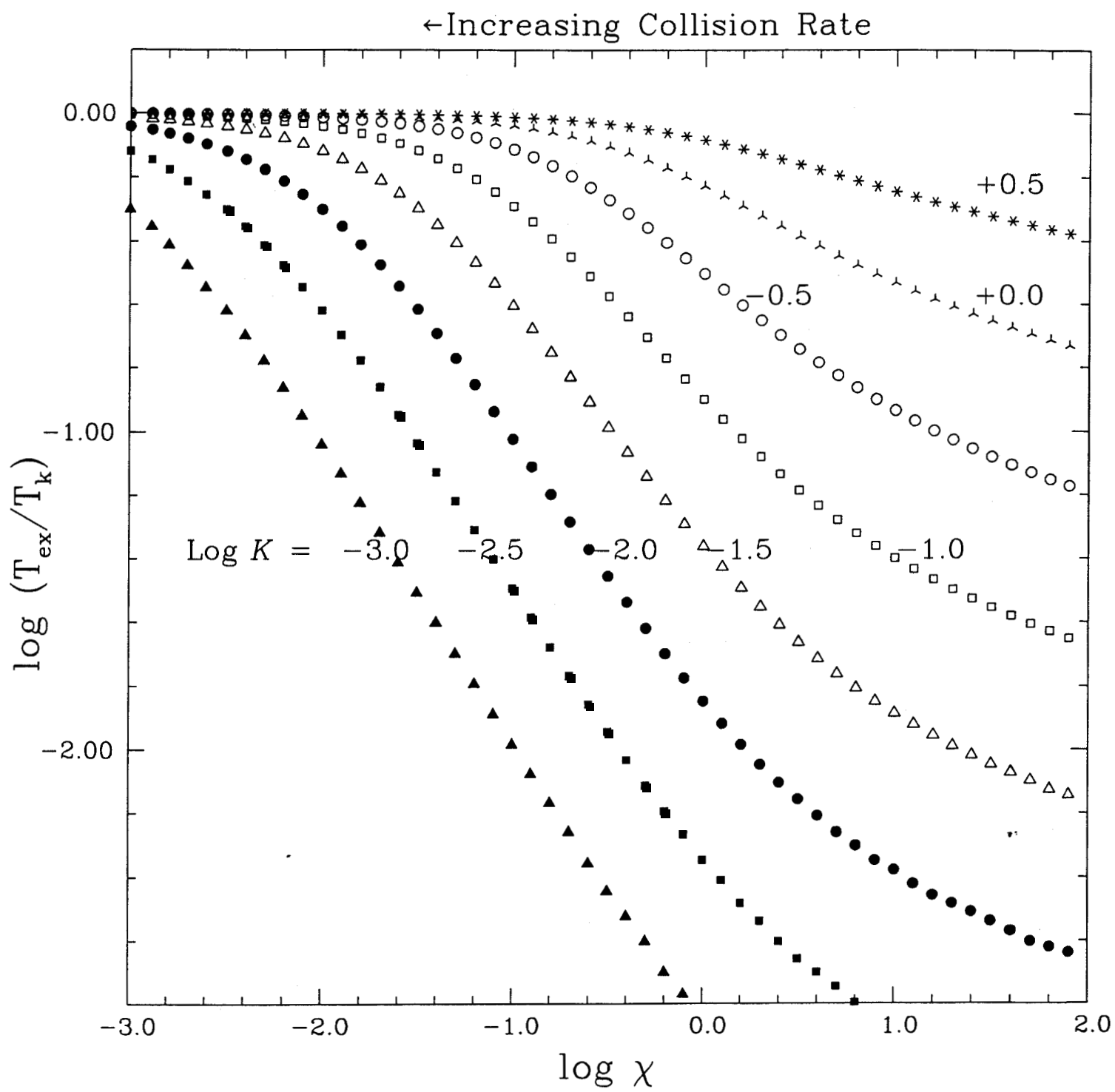
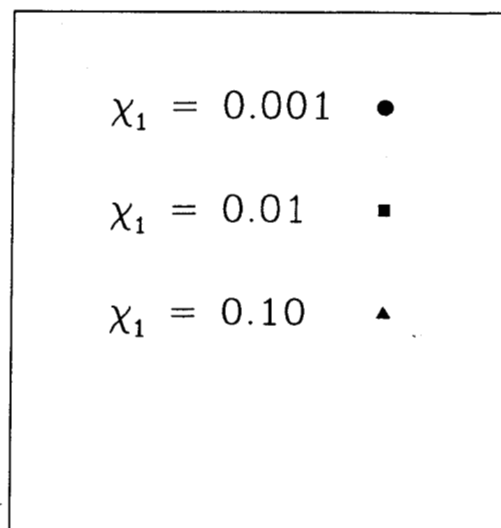
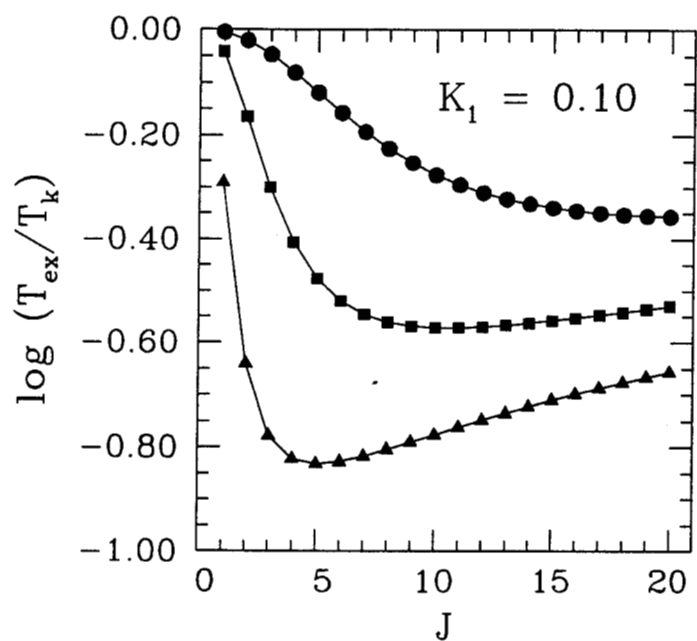
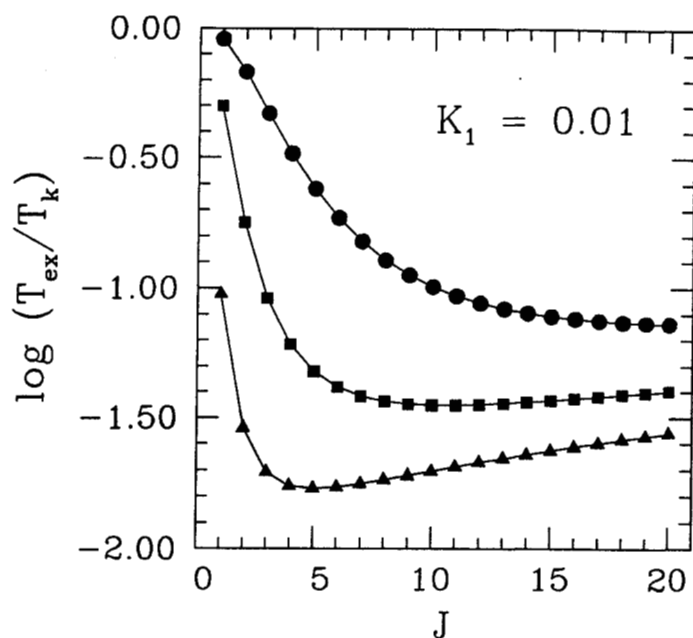
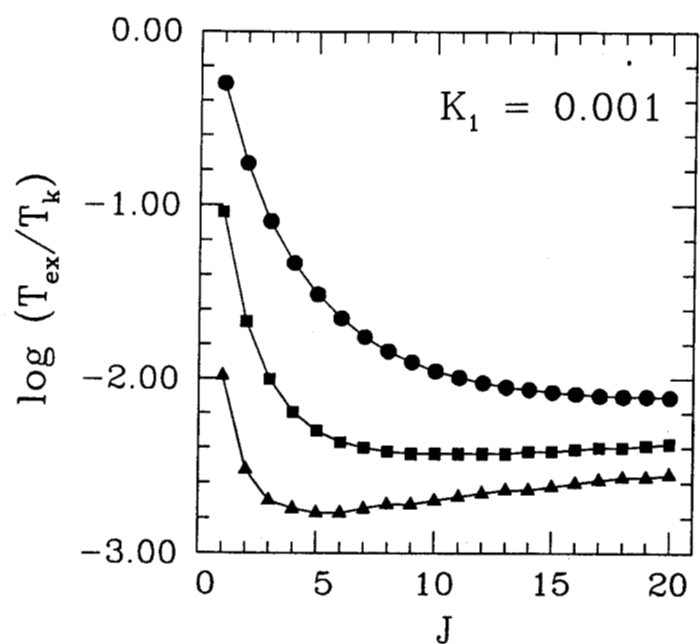


Fig A1



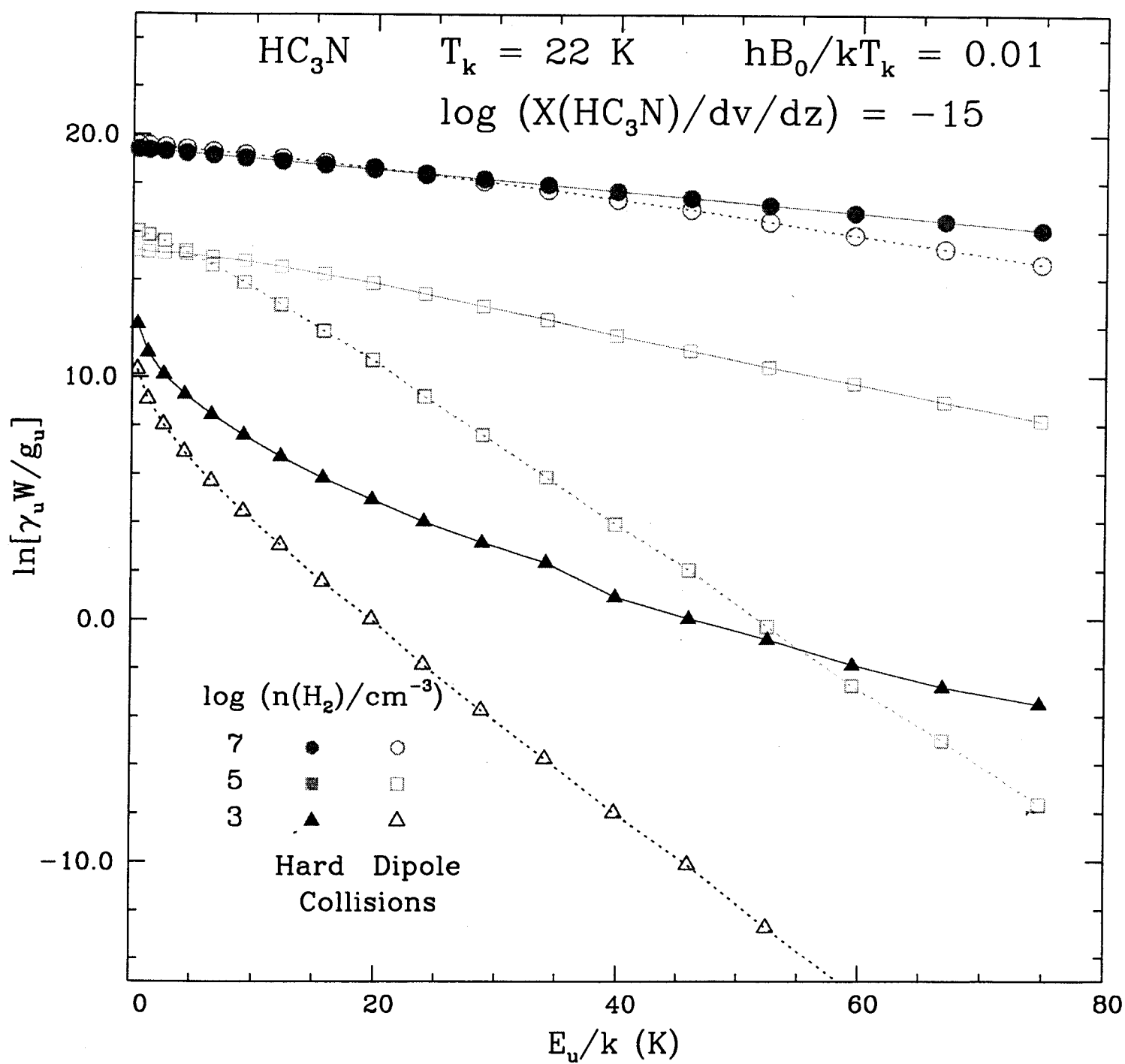


Fig A3